Title
Studies of fast electron transport in the problems of inertial fusion energy

Author
Frolov, Boris K.

Publication Date
2006

UNIVERSITY OF CALIFORNIA, SAN DIEGO

Studies of Fast Electron Transport
in
the Problems of Inertial Fusion Energy

A dissertation submitted in partial satisfaction of the
requirements for the degree Doctor of Philosophy

in

Engineering Sciences (Engineering Physics)

by

Boris K. Frolov

Committee in charge:

Sergei I. Krasheninnikov, Co-chair
Farhat Beg, Co-chair
Steven Buckley
Farrokh Najmabadi
Valentin I. Shevchenko

2006

The dissertation of Boris K. Frolov is approved, and it is acceptable in quality and form for publication on microfilm:

Co-chair

Co-chair

University of California, San Diego

2006

TABLE OF CONTENTS

LIST OF FIGURES

ACKNOWLEDGEMENTS

I would like to thank Prof. S.I. Krasheninnikov and Dr. A.Yu. Pigarov for all their help, patience and vote of confidence during my graduate studies.

The text of Chapter 2, in full, includes material from “Heat flux calculation in the semi-collisionless regime for substantial temperature variations including magnetic field” [B.K. Frolov, S.I. Krasheninnikov, R.J. Kingham and J. Edwards, New J. Phys. **8**, 56 (2006)]. The dissertation author was the primary researcher.

The text of Chapter 3, in part, includes material from “Impact of field ionization on the velocity of an ionization front induced by an electron beam propagating in a solid insulator” [B. Frolov, S. Krasheninnikov, A. Kemp, T. Cowan, New J. Phys **8**, 134 (2006)]. The dissertation author was the primary researcher.

The text of Chapter 4, in part, includes material from “The propagation of a dense relativistic electron beam through a gas” [B.K. Frolov, and S.I. Krasheninnikov, to appear in October 2006 in Phys. Plasmas]. The dissertation author was the primary researcher.

VITA

1999	B.S., Moscow Institute of Physics and Technology, Moscow, Russia.
2003	M.S., University of California, San Diego.
2006	Ph.D., University of California, San Diego.

ABSTRACT OF THE DISSERTATION

Studies of Fast Electron Transport in the Problems of Inertial Fusion Energy

by

Boris K. Frolov

Doctor of Philosophy in Engineering Sciences (Engineering Physics)

University of California, San Diego, 2006

Sergei I. Krasheninnikov, Co-chair

Farhat Beg, Co-chair

In this dissertation a systematic study of transport by super-thermal electrons in matter, using the kinetic theory and numerical simulation, is presented. This work can be divided into three major parts. The first part studies the electron thermal transport in a semi-collisionless plasma, which is also known as nonlocal transport. It was found that the nonlocal transport can be well described using a hydrodynamic framework, improved by adding a new parameter describing the energy distribution tail. For the case of a strong B-field, the accurate description of the nonlocal electron heat flux can be achieved by using an integral expression for the heat flux derived from the approximate solution of the kinetic equation.

The second and third parts of this work study the ionization wave induced by the intense electron beam propagating in different insulators. First, we study beam propagation in a solid insulator and find a non-monotonic ionization front velocity dependant on the beam density. This front velocity variation with the density can create instabilities seen in experiments. Second, we study the ionization wave in a gas induced by a dense beam. We find that, in agreement with experimental data, the ionization front velocity is much less then the beam electron velocity for low gas densities, and that the front velocity exponentially increases with the gas density.

1

Introduction

1.1 Introduction to inertial fusion

In the recent years the need for alternative sources of energy has became more and more apparent. The two main reasons are that the fossil fuel burning has strong negative side effects on the ecology and climate, and that the remaining reserves of fossil fuel appear quite limited. The known alternative sources of energy such as hydroelectric, wind or solar plants are limited in their energy output by the weather conditions in the given region in a given time period. The discovery of the fusion reactions, the most relevant for the commercial energy production of which is

$$\mathrm{D} + \mathrm{T} \rightarrow {}^{4}\mathrm{He}(3.5\,\mathrm{MeV}) + \mathrm{n}(14.1\,\mathrm{MeV})\,, \tag{1.1}$$

provided the theoretical possibility of a large scale steady generation of a clean energy. However, the fusion reaction requires the reactant (hydrogen isotopes) temperatures to be on the order of 10 keV, making it difficult to attain and sustain the high density of the reactants needed for a high reaction rate. In the existing natural fusion reactors, stars, the gravity holds the hot plasma together, however, gravity is too weak at smaller scales.

Currently, there are two different approaches to the construction of the fusion reactor. In the magnetic confinement approach [1] the B-field holds ‘burning’ fusion fuel together, theoretically allowing for the steady energy output. In the second approach, inertial confinement, the energy is produced in a series of small explosions and no long-term confinement is required. This work is focused on the problems related to the inertial confinement fusion (ICF) [2].

To achieve ignition in ICF the fuel has to be compressed to thousand times solid density (which can be accomplished using a wide variety of drivers from lasers to proton beams), because that allows the collisional trapping of some of the energetic reaction products resulting in self-heating process. The high compression ratio cannot be achieved if the compression is not symmetric (e.g. due to a nonuniform energy deposition from the driver combined with the Raleigh-Taylor-type instability [3]) or if the bulk plasma experiences excessive preheating. The numerical simulations are widely used to assess the resulting plasma temperature and pressure profile as well as energy gain. Such simulations usually involve solving a system of hydrodynamic equations for electrons and ions implicitly assuming a low ratio of the charged particle mean free path to the characteristic space scale [4]. However, this high collisionality approximation is not very accurate for fusion experiment conditions, where the laser spot size is a few tens of microns and the plasma temperature is about 1-2 keV, which corresponds to the electron and ion mean free path of about ten microns (for electron density 10^{21}cm^{-3}). After reviewing all the possible approaches to this problem we developed two modifications of the hydrodynamic set of equations designed to improve the accuracy of simulations under laser fusion conditions. The main idea of modifications is briefly outlined in Chapter 1.2.1 and the full derivation and discussion of the methods follow in the Chapter 2.

The success in the generation of ultra-intense laser pulses using the chirped pulse amplification technique [5] in the last decade has made the modification of the original laser fusion design, called Fast Ignition, look very promising. In the Fast Ignition approach [6] the fuel is not compressed as much as in the conventional approach, and the ignition happens when the additional ultra-intense driver pulse strikes an already compressed target. By decreasing the initial compression, the impact of the instabilities is also decreased. However, the key issue in the Fast Ignition becomes the delivery of the energy of the ignition pulse to the compressed target core. If a powerful laser is used as a driver then it deposits its energy in the low density plasma cloud surrounding the compressed fuel and generates the electron beam carrying the large fraction of the initial laser energy. If the beam can travel a few hundred microns to the core of the compressed fuel the sufficient beam energy can ignite it. It was observed in the experiments that the beam propagation can be inhibited by beam instabilities, such as filamentation instability [7], which dissipates directed beam energy into transverse electron heating and the B-field. It is important to understand what causes the experimentally observed instabilities and how important they would be for real fusion reactor conditions. The analysis of one of the recent experiments [8, 9] has shown that the ionization processes could be one of the reasons for the observed beam filamentation. First, we build the model of the ionization wave induced by the relativistic beam in a solid insulator corresponding to the experiment [9] and confirm the possibility of the instability induced by E-field ionization. The derivation and the results for the beam in the solid insulator model are presented in

Chapter 3. Second, we develop the collisionless ionization wave model for a beam in a gas which explains the slow beam propagation in a gas observed in the experiments with ultra-high intensity laser [10]. The model describing beam propagation in a gas is given in Chapter 4.

1.2 Outline of the dissertation

1.2.1 Chapter 2: Nonlocal transport

In ICF the plasma is often characterized by the large ratio (larger than 0.01) of the mean free path to the characteristic space scale. In the presence of a temperature gradient the induced semi-collisionless transport will cause the energy distribution function to deviate from the Maxwellian distribution (assumed in the hydrodynamic model) at its tail. In this case the hydrodynamic expression for the heat flux becomes inaccurate since the heat flux is determined predominantly by electrons from the distribution tail with energies above ~5T, where T is the electron temperature. Therefore, we consider an extension of the hydrodynamic approach which includes a new parameter allowing more accurate description of the electron distribution in the semi-collisionless regime. The other approach considered is to find the approximate form of the nonlocal (determined by distributions in the surrounding regions) electron distribution function and use it to calculate the heat flux.

A number of different approaches for description of plasma evolution have been developed over the years. The most famous ones are the Grad's 13 and 26 moment equations. We begin Chapter 2 by reviewing these methods of the heat flux calculation.

Then, in the first half of the Chapter 2, we extend the hydrodynamic approach to improve the accuracy of heat transport calculations in the absence of the B-field. A new parameter and the corresponding evolution equation are introduced into the regular hydrodynamic model to describe the evolution of the tail of the isotropic part of the electron distribution. The self–consistent E-field is found from the zero current condition. The resulting model is relatively easy to implement and shows a good agreement with kinetic simulations for up to $k\lambda_{ei} < 0.3$, where k is the inverse temperature variation length and λ_{ei} is the electron mean free path. In the second half of the Chapter 2 we exploit the fact that the distribution function is close to the Maxwellian for thermal electrons and solve the kinetic equation (including the B-field) for super-thermal tail. The resulting approximate solution allows us to find the expression for the heat flux across the B-field in the integral form. To simplify the flux calculation we account for the ambipolar field by including two normalization constants (whose values are defined against Fokker-Planck simulations) that account for the E-field effects and the B-field impact on the non-local E-field. This semi-analytical approach closely recovers the results of heat transport kinetic simulations in a wide range of collisionality and magnetization providing the way to account for the nonlocal transport across a magnetic field in existing hydrocodes.

1.2.2 Chapter 3: Beam propagation in solid insulators

In this Chapter we analyze the propagation of a high energy density (defined as the product of the beam electron energy and beam density) electron beam through a solid density insulator. The speed and structure of the ionization wave (supplying the return current electrons) created by the beam are found using the 1D steady propagation approximation. For small beam energy densities the front speed is limited by collisional ionization and decreases when going to higher beam densities (due to reduction in the beam Debye length). However, when the beam energy density exceeds a certain threshold, which is about 1% of the E-field energy density in the atom ($E_a^2/8\pi$, where $E_a = 5.1 \cdot 10^9\, V/cm$ for hydrogen), the ionization front speed increases due to the field ionization contribution. The contribution from the field ionization starts to fall when the induced E-field becomes strong enough to neutralize itself (through field ionization followed by self-consistent charge neutralization). The resulting S-shape dependence of the ionization front velocity on the beam allows for the development of filamentation type instabilities. The effect of the polarization current (caused by the E-field removing electrons from atoms) on the magnitude of the ionization front velocity though is noticeable but does not change the qualitative picture derived when neglecting it. The results from the recent numerical modeling of beam propagation in insulators [11, 12] using Vlasov-Fokker-Planck and PIC codes are consistent with the developed model. In simulations the large amplitude E-field generated by the beam was observed and the importance of both the E-field ionization and collisional ionization was confirmed.

1.2.3 Chapter 4: Beam propagation through a gas

In the last chapter of this dissertation we study the ionization front induced by a relativistic high-density electron beam propagating in a gas in 1-D approximation. We find that for low gas densities the ionization front velocity is much less than the beam electron speed. The reason is that the front velocity strongly depends on the gas density due to the exponential dependence of the field ionization rate on the induced E-field in the absence of collisional ionization. The approximate analytical expression describing the ionization front parameters is found for a wide range of gas densities and beam energies. Finally, the values of the front velocity and beam density are calculated by solving the coupled electron kinetic and Poisson's equations numerically. The calculated values of the front velocity are in a good agreement with the experimental data.

1.3 Bibliography

[1] A. H. Boozer, *Rev. Mod. Phys.* **76**, 1071 (2004)

[2] J. D. Lindl, *Phys. Plasmas* **2**, 3933 (1995); M.G. Haines, *Astrophys. Space Sci.* **256**, 125 (1998)

[3] H. Takabe, L. Montierth, and R.L. Morse, *Phys. Fluids* **26**, 2299 (1983)

[4] S. I. Braginskii, *Transport Processes in a Plasma,* in Review of Plasma Physics, Leontovich M A (ed.), New York: Consultants Bureau, Vol.1 (1965)

[5] D. Strickland, and G. Mourou, *Opt. Commun.* **56**, 219 (1985)

[6] M. Tabak, J. Hammer, M. E. Glisky, W. L. Kruer, W. C. Wilks, and R. J. Mason, *Phys. Plasmas* **1**, 1626 (1994)

[7] M. Honda , J. Meyer-ter-Vehn, and A. Pukhov, *Phys. Rev. Lett.* **85**, 2128 (2000); M. Tatarakis, F. N. Beg, E. L. Clark, A. E. Dangor, M. S. Wei, P. A. Norreys, M. Zepf, K. W. D. Ledingham, T. J. Goldsack, R. D. Edwards and K. Krushelnick, *Phys. Rev. Lett.* **90**, 175001 (2003)

[8] S. Krasheninnikov, A. V. Kim, B. K. Frolov, R. Stephens, *Phys. Plasmas* **12**, 073105 (2005)

[9] R. Stephens R. A. Snavely, Y. Aglitskiy, F. Amiranoff, C. Andersen, D. Batani, S. D. Baton, T. Cowan, R. R. Freeman, T. Hall, S. P. Hatchett, J. M. Hill, M. H. Key, J. A. King, J. A. Koch, M. Koenig, A. J. MacKinnon, K. L. Lancaster, E. Martinolli, P. Norreys, E. Perelli-Cippo, M. Rabec Le Gloahec, C. Rousseaux, J. J. Santos, and F. Scianitti, *Phys. Rev. E* **69**, 066414 (2004)

[10] D. Batani, S. D. Baton, M. Manclossi, J. J. Santos, F. Amiranoff, M. Koenig, E. Martinolli, A. Antonicci, C. Rousseaux, M. Rabec Le Gloahec, T. Hall, V. Malka, T. E. Cowan, J. King, R. R. Freeman, M. Key, and R. Stephens, *Phys. Rev. Lett.* **94**, 055004 (2005)

[11] A. P. L. Robinson, A. R. Bell, and R. J. Kingham, *Plasma Phys. Control. Fusion* **48**, 1063 (2006)

[12] A. J. Kemp, Robert E. W. Pfund, and Jürgen Meyer-ter-Vehn, *Phys. Plasmas* **11**, 5648 (2004); A. J. Kemp, Y. Sentoku, T. Cowan, J. Fuchs, and H. Ruhl, *Phys. Plasmas* **11**, L69 (2004).

2

Nonlocal Transport

2.1 Problem overview

The most promising approach to Inertial Confinement Fusion (ICF) [1-3] is Fast Ignition, in which the set of lasers is used to compress the ~1 mm DT (deuterium-tritium) pellet into ~0.1 mm dot, and then ultra-high intensity single laser is used to ignite the compressed fuel. The large amount of data from numerous experiments and different theories can be directly compared using numerical simulations. In spite of all new and different approaches to the plasma simulation (e.g. based on quasi-particles like in PIC codes [4-7], or based on the solution of the Boltzman-Fokker-Planck equation [8]) the old hydrodynamic approach still widely used. The reason for such resilient popularity is the speed and the simplicity of the code. The prohibitive computational time cost of the kinetic codes makes the hydrocodes the tool of choice for full-scale modeling. In this Chapter we are extending the scope of applicability of the hydrodynamic approach by introducing new expressions for the heat flux which are more accurate in the semi-collisionless fusion plasma.

In the hydrodynamic approach instead of specifying the position and velocity of each particle with mass m, we use the set of 'velocity moments' (density n, average velocity, temperature T) of the electron and ion distributions to describe plasma. These quantities are defined as integrals of the distribution function (normalized to the particle density) multiplied by the appropriate power of the velocity, i.e. (1, $\mathbf{v}/n$, $mv^2/2n$) correspondingly, over the velocity space. Usually, the description of the plasma assumes that the velocity distribution function is Maxwellian, and, therefore, this description of plasma breaks down when the electron distribution function substantially deviates from the Maxwellian distribution (from that point on we will be talking only about electrons since their diffusion coefficient is $(m_i/m)^{1/2}$ times larger than that of ions, assuming that ion and electron temperatures are equal; m_i and m are the ion and electron masses). The Maxwellian distribution corresponds to the state of a local equilibrium which implies the smallness of the electron free path between collisions compared to the space scale L of any variation. Most of the electrons have the collisional free path close to the mean free path $\lambda_{ei} = \tau_{ei}\sqrt{2T/m}$, where $\tau_{ei} = 3\sqrt{m}T^{3/2}/(4\sqrt{2\pi}Z\Lambda e^4 n)$ is the electron mean collision time; Λ is the Coulomb logarithm; e and T are the electron charge and temperature; n is the electron density; Z is the ion charge number. Therefore if $k\lambda_{ei} \lesssim 10^{-1}$, where $k = 2\pi/L$, the most of the electrons experience on average more than 10 collisions before they reach a region where the value of the distribution function parameters are substantially different. These collisions bring the incoming particles into local equilibrium with others. If however we consider the process of heat transport we find that the contribution to the heat flux comes mainly from electrons with energy $\varepsilon \sim 5T$ (in the absence of magnetic field) whose free path is much larger. That can be understood as follows. The electron diffusion coefficient (for electrons with energy $\varepsilon = mv^2/2$) is approximately $D_e(\varepsilon) \approx \varepsilon\tau(\varepsilon)/m$, with $\tau \propto \varepsilon^{3/2}$, and the energy diffusion flux is approximately $\varepsilon D_e \partial f/\partial x$, where f is the electron distribution function (EDF) whose integral over the whole velocity space gives us the electron density. We integrate the energy flux over all velocities to obtain the integral heat flux $q \propto \int \exp(-\varepsilon/T)\varepsilon^5 d\varepsilon$, where we assumed that f is Maxwellian. The expression under the integral strongly peaks at $\varepsilon = 5T$. Therefore we can use the hydro model to describe the heat transport (classical Spitzer-Harm expression for the heat flux [9,10]) only if electrons with $\varepsilon \sim 5T$ can reach equilibrium on the space scale smaller than the inhomogeneity space scale L. The time of energy equilibration is about the time between electron-electron collisions but the distance traveled by an electron within that time is limited by its diffusion through ions and we find that energy equilibration length is $\lambda_T = \lambda_{ei}\sqrt{Z}$. Therefore if we want to use the hydrodynamic approach to describe the heat transport the energy equilibration length λ_T of electrons with $\varepsilon \sim 5T$ has to be much smaller than the temperature variation length L, which amounts to $k\lambda_T \lesssim 10^{-2}$. For a very short wavelength inhomogeneity of electron temperature, $k\lambda_T > 10^{-2}$, the 'tail' electrons with $\varepsilon \sim 5T$ propagate far ($\lambda_T > L$) without equilibrating and their distribution function may strongly depart from the Maxwellian.

Thus, for the heat flux calculation we only need to know the EDF around $\varepsilon \sim 5T$ (for the case of no magnetic field), where the main portion of the heat flux is carried on [11], and the knowledge of the full distribution is rather excessive. Therefore, one can improve the accuracy of the hydrodynamic description of the heat flux for $k\lambda_T \gtrsim 10^{-2}$ by using one additional parameter W, along with the electron density and temperature, for more accurate description of the tail distribution around $\varepsilon \sim 5T$. Some approaches [12-14] to the calculation of the nonlocal heat flux are based on the finding of the *full* energy distribution which significantly complicates the solution. On the other hand in the linear Grad's method [15-17] only 2 scalar moments (corresponding to the convolutions of EDF with $\{1, v^2\}$) are used for the description of the isotropic part of the EDF, which, thus, is always Maxwellian. In the Section 2.2 we develop the approach to improve the accuracy of a hydrodynamic calculation of the heat flux for $0.01 \lesssim k\lambda_T \lesssim 1$. For $k\lambda_T \gtrsim 1$ and large temperature variations the EDF is strongly non-Maxwellian and, generally, no conveniently small set of macro parameters can describe the particle transport. However, there are works [18-19] which describe the heat flow in plasma using a moment method for special cases, e.g. 2 walls configuration, for arbitrary $k\lambda_{ei}$. It is worth noting that approach of 'additional parameter' to calculation of the nonlocal heat flux is not limited to small temperature perturbations $\delta T << T$ which have been extensively studied in a number of papers (e.g. see Ref. [20-21]).

The alternative approach to the heat flux which accounts for the kinetic effects is the nonlocal approach [22-23], where the limit on the temperature profile steepness improves to $k\lambda_{ei} < 1$ due to the assumption that the isotropic part f_0 of the EDF is Maxwellian only for $\varepsilon / T \lesssim 1$, while for the super-thermal electrons with $\varepsilon / T >> 1$ f_0 is found from the solution of the Boltzmann kinetic equation. This approach has been implemented in a number of works [12,13,21-23] for the case of no magnetic field. However, in many cases including the inertial and magnetic fusion and astrophysics the magnetic field effects play an important role in the electron heat conduction (see for example [20,24,25]). Magnetic field effects on the nonlocal heat flux were considered in

[20], but only for small temperature perturbations $\delta T << T$. Therefore, in Section 2.3 we extend the results obtained in [12,13] to incorporate the impact of the magnetic field on the nonlocal electron heat transport.

In magnetized plasma, $\lambda_{ei} / \rho_{Be} >> 1$, the electron cyclotron radius $\rho_{Be} = (2T/m)^{1/2} / \omega_B$ replaces the mean free path as a characteristic transport scale (here $\omega_B = |e| B/(mc)$ is the electron cyclotron frequency; B is the magnetic field strength; and c is the light speed), and the main contribution to the heat flux comes from electrons with energy around 2T for $\lambda_{ei} / \rho_{Be} >> 1$, because the electron diffusion coefficient gets much smaller for higher ε, i.e. $D_e(\lambda_{ei} /(\omega_B \tau_{ei})^2) \approx v\lambda_{ei} /(\omega_B \tau_{ei})^2 \propto \varepsilon^{-1/2}$ (instead of $\varepsilon^{5/2}$) and the integral heat flux $q \propto \int \exp(-\varepsilon / T)\varepsilon^2 d\varepsilon$. (Note: If one would account for the return current the maximum contribution would shift approximately to $\varepsilon \sim 6.5T$ and $\varepsilon \sim 2.5T$ for the cases $\lambda_{ei} / \rho_{Be} << 1$ and $\lambda_{ei} / \rho_{Be} >> 1$, correspondingly). The classical approach for the heat flux across homogeneous B-field remains valid as long as $k\rho_{Be} << 1$ [24], even for large $k\lambda_{ei}$. In the Section 2.3 we find an expression for the heat flux across a magnetic field with the limit of applicability extended to

$$\min(\lambda_{ei}, \rho_{Be}) < 1/k, \tag{2.1.1}$$

without limiting the scope of the problem to small perturbations of the plasma temperature.

We summarize the results from two different approaches and draw the conclusions in the Section 2.4.

2.2 Additional parameter model

2.2.1 Governing equations

We start with the Boltzmann kinetic equation for electrons without magnetic field (which is simply the continuity equation in 6 dimensional space (3D + 3V) for the EDF, describing the density of electrons with given velocity)

$$\partial_t f + \mathbf{v} \cdot \nabla f - (e\mathbf{E}/m) \cdot \nabla_{\mathbf{v}} f = C_{ee} + C_{ei}, \tag{2.2.1}$$

where E is the electric field; C_{ee} and C_{ei} are the electron-electron and electron-ion collision terms, correspondingly. We use the approximate form of C_{ei} and C_{ee} from Ref. [24]

$$C_{ei} \approx \frac{2\pi\Lambda e^4 nZ}{m^2} \frac{\partial}{\partial v_\alpha} \left[\frac{v^2 \delta_{\alpha\beta} - v_\alpha v_\beta}{v^3} \frac{\partial f}{\partial v_\beta} \right],$$

$$C_{ee}(\varepsilon / T >> 1) \approx \frac{2\pi\Lambda e^4 n}{m^2} \frac{\partial}{\partial v_\alpha} \left(\frac{2v_\alpha}{v^3} f + \frac{T}{m} \frac{3v_\alpha v_\beta - v^2 \delta_{\alpha\beta}}{v^5} \frac{\partial f}{\partial v_\beta} \right).$$

We approximate the EDF with a truncated spherical harmonics expansion (so called "diffusive approximation") [8]

$$f(t,\mathbf{x},\mathbf{v}) = f_0(t,\mathbf{x},|\mathbf{v}|) + \mathbf{b}(t,\mathbf{x},|\mathbf{v}|) \cdot \mathbf{v}. \tag{2.2.2}$$

The anisotropic part of the EDF $\mathbf{b} \cdot \mathbf{v}$ reaches equilibrium through electron–ion collisions, which are Z times more frequent than the electron-electron collisions responsible for the energy distribution f_0 equilibration. Therefore, for slow time variations $\partial(\mathbf{b} \cdot \mathbf{v}) / \partial t << (\mathbf{b} \cdot \mathbf{v}) \cdot \nu_{ei}$ we neglect $\partial(\mathbf{b} \cdot \mathbf{v}) / \partial t$ term in Eq.(2.2.1), but keep $\partial f_0 / \partial t$ term. Taking the 0th and 1st angular moments of Eq.(2.2.1) (multiply by 1 and $\mathbf{v}/|\mathbf{v}|$ and integrate over the full solid angle) we obtain the set of two different equations relating $\mathbf{b}$ and f_0

$$\nabla f_0 - e\mathbf{E}\frac{\partial f_0}{\partial \varepsilon} = -\frac{\mathbf{b}}{\tau_p}, \tag{2.2.3}$$

$$\frac{\partial f_0}{\partial t} + \frac{2\varepsilon}{3m}\nabla \cdot \mathbf{b} - \frac{e\mathbf{E}}{m}\frac{2}{3\sqrt{\varepsilon}}\frac{\partial}{\partial \varepsilon}\left(\varepsilon^{3/2}\mathbf{b}\right) = C_{ee}. \tag{2.2.4}$$

From Eq.(2.2.3) we obtain the expression for vector **b**

$$\mathbf{b} = -\tau_p\left[\nabla f_0 - e\mathbf{E}\frac{\partial f_0}{\partial \varepsilon}\right],$$

where $\tau_p = \tau_{ei}(\varepsilon/T)^{3/2}4/(3\sqrt{\pi})$ came from C_{ei} term, and after the substitution of Eq.(2.2.3) into Eq.(2.2.4) we can get the equation for f_0. We have not done anything new yet, basically up to this point we followed the footsteps of Braginskii [24]. Now we write f_0 as a sum of $f_M(t,x,\xi)$ and the correction function $W(t,x)\cdot P_S(\xi)\cdot f_M(t,x,\xi)$

$$f_0(t,x,\xi) = C_M(t,x)\exp(-\xi)\left[1 + W(t,x)P_S(\xi)\right], \tag{2.2.5}$$

where $\xi = \varepsilon/T$; $C_M(t,x) = n(m/2\pi T)^{3/2}$; $P_S(\xi)$ is a some function of ξ, the subscript 'S' points at functions and variables which values depend on the choice of function P_S . The new parameter W allows us to correct the 'tail' of the EDF without changing the particle density and the average energy. The equation for the Nth energy moment of f_0

$$M^{(N)} \equiv \int f_0\varepsilon^N d^3v = nT^N \cdot H^{(N+1/2)}2/\sqrt{\pi}, \tag{2.2.6}$$

where $H_S^{(N)} \equiv \int e^{-\xi}(1 + W\cdot P_S)\xi^N d\xi = \Gamma(N+1) + W\cdot J_S^{(N)}$; $\Gamma(y)$ is the gamma function; $J_S^{(N)} \equiv \int e^{-\xi}\xi^N P_S(\xi)d\xi$; is obtained by integrating Eq.(2.2.4) multiplied by ε^N over the velocity space

$$\frac{\partial M^{(N)}}{\partial t} + \frac{\partial A_{\beta C}^{(N+1)}}{\partial x_\beta} + NA_{\beta C}^{(N)}eE_\beta = \int C_{ee}\varepsilon^N d^3v, \tag{2.2.7}$$

where

$$A_\beta^{(N)} \equiv \frac{2}{3m}\int b_\beta \varepsilon^N d^3v = -\frac{\sqrt{\pi}C_A}{2n}\left[\frac{\partial M^{(N+3/2)}}{\partial x_\beta} + (N+2)eE_\beta M^{(N+1/2)}\right], \qquad (2.2.8)$$

$$C_A \equiv \frac{16}{9\pi}\frac{Z}{Z+1}\frac{n\tau_{ei}}{mT^{3/2}}, \quad \int C_{ee}\varepsilon^N d^3v = \begin{bmatrix} 0, & \text{for } N=0,1 \\ -WnT^N\nu_W^N, & \text{for } N>1 \end{bmatrix}, \qquad (2.2.9)$$

where $\nu_W^N = 3N\left[J_S^{(N-1)} - (N-1)J_S^{(N-2)}\right]/(\tau_{ei}Z)$. The factor Z/(Z+1) in the expression for C_A comes from the electron-electron collisions happening on the timescale of τ_{ei}/Z. These collisions increase the effective 'collisional' ion charge by one. To calculate the integral in Eq.(2.2.9) with N>1 we have used the high energy (ε/T>>1) approximation for C_{ee} from Ref. [24] introduced earlier, since the main contribution into the value of the integral in this case (N>1) is coming from high energies. The vector $\mathbf{A}^{(N)}$ is the flux of the (N-1)th energy moment, e.g. $\mathbf{A}^{(1)}$ is the electron flux, $\mathbf{A}^{(2)}$ is the heat flux. Assuming that there is no electron current we get $\mathbf{A}^{(1)}$=0, and find the expression for the electric field from Eq.(2.2.8) using N=1

$$eE_\beta = \frac{-1}{3M^{(3/2)}}\frac{\partial M^{(5/2)}}{\partial x_\beta}. \qquad (2.2.10)$$

To make the particle density and the average energy independent of W we require that the correction function $P_S(\xi)$ satisfies

$$J_S^{(N)}=0 \text{ for } N=1/2,\ 3/2, \qquad (2.2.11)$$

i.e. $M^{(0)}$=n, $M^{(1)}$=1.5nT. This way the transport coefficients and fluxes depend on the parameter W and its derivatives but the values of n and T are independent of W.

The function f_0 is determined by three variables n(t,x), T(t,x), W(t,x), and the three corresponding evolution equations (for 0th, 1st, and Lth moments of f_0) in 1D case (and in the absence of the electron current) are obtained from Eq.(2.2.7)

$$\frac{\partial n}{\partial t} = 0,$$

$$\frac{\partial T}{\partial t} = \frac{-1}{1.5n}\frac{\partial A^{(2)}}{\partial x}, \tag{2.2.12}$$

$$\frac{\partial W}{\partial t} = \frac{-\sqrt{\pi}}{2J_S^{(L+1/2)}}\left\{\frac{2L}{\sqrt{\pi}}H_S^{(L+1/2)}\frac{\partial \ln T}{\partial t} + \frac{1}{nT^L}\left[\frac{\partial A^{(L+1)}}{\partial x} + LA^{(L)}eE\right] + \nu_W W\right\},$$

where L>1; $\nu_W \equiv \nu_W^L$ is the decay rate of W due to collisions. (Note: The presence of an electron current would add few terms in Eq.(2.2.12) which, if needed, could be found from Eq.(2.2.7-8).)

The rate of Maxwellization of super thermal electrons with ε/T~5 is much slower than for electrons with $\varepsilon/T{\sim}1$, $\nu_W << 1/\tau_{ee}$. And, though, we limit the rate of change of W, $\partial W/\partial t << W/\tau_{ee}$, to have f_0 not far from f_M, we keep $\partial W/\partial t$ term because it is possible that $\partial W/\partial t \sim \nu_W W$. If we set $\partial W/\partial t = 0$ we would obtain the quasi equilibrium model, somewhat similar to the nonlocal models [12,13], describing the heat flux when the non-Maxwellian hot 'tail' electron 'fluid' is already in equilibrium across the temperature gradient while the thermal electrons with $\varepsilon/T \approx 1$ are not.

The approximate analytical solution of the system in Eq.(2.2.12) for small perturbations presented in the following section reveals the main features and limitations of the model, before we proceed to the numerical modeling of Eq.(2.2.12) in the Section 2.3.

2.2.2 Linear analysis

In this section we apply our model to the decay of a small temperature perturbation to find the linear decay rate. The (N-1)th moment flux $A^{(N)}$ given in Eq.(2.2.8) can be rewritten as

$$A^{(N)} = -C_A \cdot T^{N+3/2}\left[\frac{\partial \ln n}{\partial x}K_n^{(N)} + \frac{\partial W}{\partial x}K_W^{(N)} + \frac{\partial \ln T}{\partial x}K_T^{(N)}\right], \qquad (2.2.13)$$

where

$$\begin{aligned} K_n^{(N)} &= H_S^{(N+2)} - \frac{(N+2)}{3}\frac{H_S^{(N+1)}H_S^{(3)}}{H_S^{(2)}}, \\ K_T^{(N)} &= H_S^{(N+2)}\left(N+\frac{3}{2}\right) - \frac{5}{2}\frac{(N+2)}{3}\frac{H_S^{(N+1)}H_S^{(3)}}{H_S^{(2)}}, \\ K_W^{(N)} &= J_S^{(N+2)} - \frac{(N+2)}{3}\frac{H_S^{(N+1)}J_S^{(3)}}{H_S^{(2)}}. \end{aligned} \qquad (2.2.14)$$

In the linear approximation the coefficients $[C_A T^{N+3/2} K_i^{(N)}]$ (i=n, T or W) in Eq.(2.2.13) are assumed to be constant and that simplifies Eq.(2.2.12) to

$$\begin{aligned} \frac{\partial T}{\partial t} &\approx X_T \frac{\partial^2 T}{\partial x^2} + X_W \frac{\partial^2 W}{\partial x^2}, \\ \frac{\partial W}{\partial t} &\approx D_T \frac{\partial^2 T}{\partial x^2} + D_W \frac{\partial^2 W}{\partial x^2} - W \nu_W \sqrt{\pi}\,/\left(2J_S^{(L+1/2)}\right), \end{aligned} \qquad (2.2.15)$$

where X_i and D_i are the appropriate diffusion coefficients derived from Eq.(2.2.12-14)

$$\begin{aligned} X_T &= \frac{2C_A T^{5/2}}{3n}K_T^{(2)}, \quad X_W = \frac{2C_A T^{7/2}}{3n}K_W^{(2)}, \\ D_T &= \frac{\sqrt{\pi}C_A T^{3/2}}{2J_S^{(L+1/2)}n}\left(K_T^{(L+1)} - K_T^{(2)}H_S^{(L+1/2)}\frac{4L}{3\sqrt{\pi}}\right), \\ D_W &= \frac{\sqrt{\pi}C_A T^{5/2}}{2J_S^{(L+1/2)}n}\left(K_W^{(L+1)} - K_W^{(2)}H_S^{(L+1/2)}\frac{4L}{3\sqrt{\pi}}\right). \end{aligned} \qquad (2.2.16)$$

We also assumed that the amplitude of W is small so $K_n^{(N)}(W \approx 0) \approx 0$ (no contribution to the flux from the density gradient) and $X_T(W \approx 0)$ becomes the classical heat diffusivity $X_T^{\text{classic}} = 256 T \tau_{ei} / (9\pi m)$. We look for the solution of Eq.(2.2.15) in the form of decaying periodic perturbation $T = T_1 \exp(ikx - \gamma t)$ and $W = W_1 \exp(ikx - \gamma t)$. We find that the linear decay rate γ for a temperature perturbation with given k is

$$\frac{\gamma}{k^2 X_T} = \frac{1}{2}\left(\frac{D_W}{X_T} + 1 + \frac{1}{(k\lambda)^2} \pm \sqrt{\left[\frac{D_W}{X_T} - 1 + \frac{1}{(k\lambda)^2}\right]^2 + 4\frac{D_T X_W}{X_T^2}} \right), \qquad (2.2.17)$$

where $\lambda^2 = X_T / \left[\nu_W \sqrt{\pi} / \left(2 J_S^{(L+1/2)}\right)\right] = \lambda_{ei}^2 Z \cdot 256 J_S^{(L+1/2)} / \left(27 \pi^{3/2} L \left[J_S^{(L-1)} - (L-1) J_S^{(L-2)}\right]\right)$.

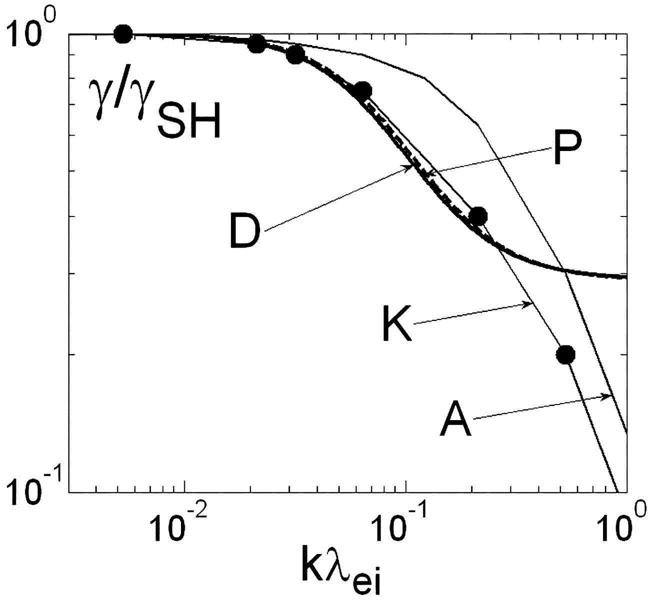

Figure 2.1 Linear decay rate of a temperature perturbation γ / γ_{SH} (ratio of the effective heat conductivity to the classical Spitzer-Harm [9,10] heat conductivity) as a function of $k\lambda_{ei}$, where k is the wave number of the perturbation and λ_{ei} is the thermal electron mean-free path. Curves ‘A’ and ‘K’ are the delocalization models from Ref. [12] and [13] respectively; filled circles relate to Fokker-Planck modeling from Ref. [26]. Curves ‘P’ and ‘D’ are the linear decay rates of the ‘additional parameter‘ model with correction functions constructed on a polynomial basis or a delta-function basis, respectively.

In the classical limit $k\lambda <<1$ collisions neutralize W and Eq.(2.2.17) recovers the classical heat diffusion decay rate $\gamma_{SH} = k^2 X_T$. In the opposite limit $k\lambda >>1$ we get $\gamma / k^2 X_T =$ const $\equiv C_\gamma$ (see Figure 2.1), $0<C_\gamma<1$, which corresponds to the maximum heat flux reduction in the absence of collisional neutralization of W. For Eq.(2.2.12) to be linearly stable one has to have $0<C_\gamma$ and that requires $X_T D_W > X_W D_T$ (which amounts to $K_W^{(L+1)} / K_W^{(2)} > K_T^{(L+1)} / K_T^{(2)}$). This expression limits the subset of possible values of L for a given correction function $P_S(\xi)$ due to a linear stability. Though we used small temperature perturbation approach to find the linear decay rate of perturbation, the model itself (based on Eq.(2.2.12)) is not limited to small perturbations. In the next section we use a test problem featuring large temperature variations and compare our results to Fokker-Planck simulations.

2.2.3 Test problem. Comparison with Fokker-Planck simulation

To start the simulation we have to choose the correction function $P_S(\xi)$ which determines the value of the coefficients $J_S^{(N)}$ (N=0,1,L) introduced after Eq.(2.2.6). The choice of $P_S(\xi)$ is quite arbitrary, and we choose it to be the sum of 3 different functions (which have finite integrals with $\exp(-\xi)\xi^{N+1/2}$, N>0) with 2 free parameters p_1 and p_2 (which we need to make $P_S(\xi)$ orthogonal to 1 and ξ with weight function $W = \exp(-\xi)\xi^{1/2}$ (see Eq.(2.2.11)))

$$P_S(\xi) = F_3(\xi) + p_2 F_2(\xi) + p_1 F_1(\xi), \tag{2.2.18}$$

where $p_2 = -(\Phi_3^{(0)} + p_1\Phi_1^{(0)})/\Phi_2^{(0)}$; $p_1 = -(\Phi_2^{(1)}\Phi_3^{(0)} - \Phi_2^{(0)}\Phi_3^{(1)})/(\Phi_2^{(1)}\Phi_1^{(0)} - \Phi_2^{(0)}\Phi_1^{(1)})$; $\Phi_n^{(k)} = \int_0^\infty F_n(\xi)\cdot e^{-\xi}\xi^{k+1/2}d\xi$. That allows us to calculate all coefficients in Eq.(2.2.12) using

$$J_S^{(k)} = \Phi_3^{(k-1/2)} + p_2\Phi_2^{(k-1/2)} + p_1\Phi_1^{(k-1/2)} \tag{2.2.19}$$

for any given set of functions $F_i(\xi)$, i=1,2,3.

If we use δ-functions to compose the correction function $P_S(\xi)$, $F_i(\xi)=\delta(\xi-S_i)$, then $\Phi_i^k = \exp(-S_i)S_i^{k+1/2}$. The relative linear decay rate γ/γ_{SH} for this case is plotted as a function of $k\lambda_{ei}$ on Figure 2.1 for $P_S(\xi) = \delta(\xi-9) + p_2\delta(\xi-1) + p_1\delta(\xi-0.5)$ for L=3 (Note: in this case the value of L=2 cannot be used since it leads to $\nu_W(L=2) = 6\left[J_S^{(1)} - J_S^{(0)}\right]/(\tau_{ei}Z) < 0$ due to Eq.(2.2.11)). By changing the values of $\{S_i\}$ one does not change the shape of the curve on Figure 2.1 but rather changes the level where it becomes flat (minimal value of γ/γ_{SH}). This set of values of S_i and L (when P_S is composed by δ-functions) seems to provide the least value of γ/γ_{SH} in the limit $k\lambda_{ei}$>>0.1 while remain stable in the simulation of the test problem described below. If the correction function is a polynomial $F_i(\xi) = \xi^{S_i}$, then $\Phi_i^k = \Gamma(S_i + k + 3/2)$. The linear decay rate γ for this case is also plotted on Figure 2.1 for $P_S(\xi) = \xi^{1.5} + p_2\xi + p_1\xi^{0.1}$ for L=3. In both cases, for $k\lambda_{ei} \gtrsim 0.5$ the model reduces to Spitzer-Harm model [9] with the flux limiter being equal to about 0.3.

We applied this heat flux calculation approach to the test problem, where we imposed a constant sinusoidal heating profile $S(x)=(3/2)S_0[1+\cos(2\pi x/L_H)]$ on an initially flat temperature profile T_0 allowing the system to develop its 'natural' temperature profile as time goes on. We followed the time evolution of the amplitude of the relative temperature peak (T_{max}-T_{min})/<T>, where <T> denotes the average temperature. The following values of other parameters were used (typical for a laser plasma): T_0=1 keV, n_e=10^{21} cm^{-3}, Z=1 (in the high Z limit approximation), L_H=2 mm, S_0=4.5 keV/ns. The value of $k\lambda_{ei}$ calculated using the average temperature increases from about 0.1 to 1 following a $<T>^2$ law, due to the quadratic temperature dependence of the mena free path (see Figure 2.2).

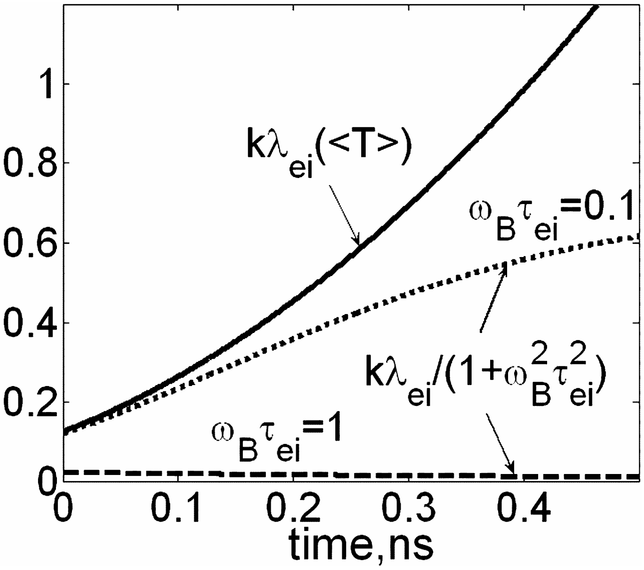

Figure 2.2 The time evolution of the 'non-locality' parameter $k\lambda_{ei}/(1+\omega_B^2\tau_{ei}^2)$ with and without a magnetic field. The value of the parameter was calculated using the space average temperature value which grows linearly in time due to the constant heating.

For the heating to be Maxwellian (i.e., to obtain a distribution of the added energy according to a Maxwellian function) values of both T and W have to change, since

$$\Delta f_0 = \frac{\partial f_0}{\partial T}\Delta T + \frac{\partial f_0}{\partial W}\Delta W = \left(\frac{\partial f_M}{\partial T} + W\frac{\partial}{\partial T}\left[f_M P_S\right]\right)\Delta T + f_M P_S \Delta W\,, \tag{2.2.20}$$

therefore, $\Delta f_0 = \Delta T \cdot \partial f_M / \partial T$ if $W\partial[f_M P_S]/\partial T \cdot \Delta T = -f_M P_S \cdot \Delta W$, which after integration with ε^L over the velocity space yields $\Delta W = -WL\Delta T/T$ (for L=0,1 it is already satisfied due to Eq.(2.2.11)). Thus, the Maxwellian heating S(x) (energy per second per particle) causes change in values of T and W simultaneously

$$\begin{bmatrix} \partial T/\partial t \\ \partial W/\partial t \end{bmatrix}_{HEATING} = \frac{S}{3/2}\begin{bmatrix} 1 \\ -L\cdot W/T \end{bmatrix}. \qquad (2.2.21)$$

For the test problem simulation we insert these heating terms into our system of equations given in Eq(2.2.12).

Using the heat transport model given by Eq.(2.2.12) we calculated the evolution of the relative temperature peak $(T_{max}-T_{min})/\langle T\rangle$ in the described test problem with the spatially modulated heating. The calculation results are plotted on Figure 2.3 for two different forms of correction function (polynomial and δ-function).

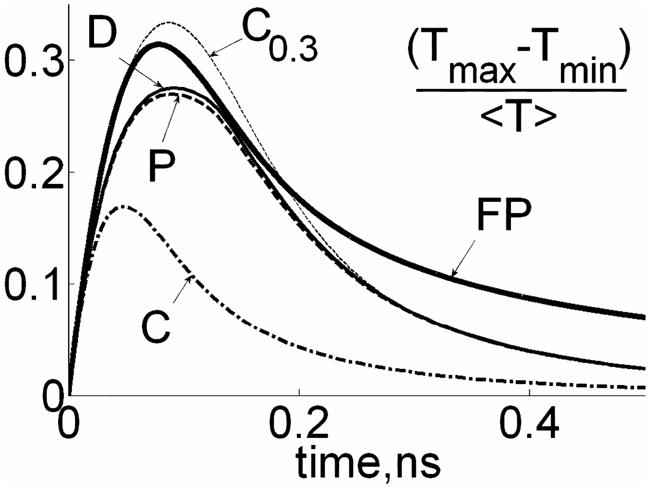

Figure 2.3 Time evolution of $(T_{max}-T_{min})/\langle T\rangle$ according to the classical [9,10] theory ('C' curve), the 'additional parameter' model ('P' and 'D' curves correspond to the polynomial correction function and the function made of delta-functions, respectively) and the results from the IMPACT kinetic code [8] ('FP' curve). Curve '$C_{0.3}$' refers to the classical model with the flux limiter 0.3.

As one would expect from the analysis of Figure 2.1 the polynomial and δ-functions descriptions are very similar and provide a rather good fit (less than 15% difference) to the Fokker-Planck (FP) simulation data (obtained using IMPACT code [8]) but only for $k\lambda_{ei} < 0.3$. For $k\lambda_{ei} > 0.3$ the model behaves as the classical hydro model with the flux limiter 0.3 (see Figures 2.1 and 2.3). In the test problem $k\lambda_{ei}$ reaches 0.3 at $t \approx 0.15$ ns (see Figure 2.2) and according to the linear analysis our model starts to depart from the FP data [8].

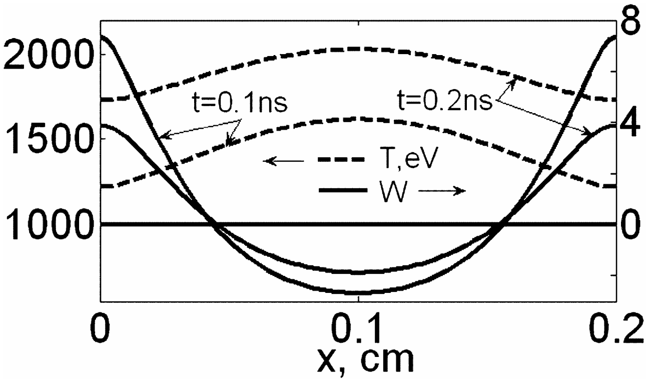

Figure 2.4 Space profiles of T and W for two different times: 0.1 ns and 0.2 ns. Initial profiles are flat with T_0=1000 eV and W_0=0. The amplitude of W initially grows for ~0.1 ns and then fades away to 0 (as T profile flattens).

The space distribution of T and W are plotted on Figure 2.4 for t = 0.1 and 0.2 ns. Initially T is set to 1000eV and W is set to be zero everywhere. As time goes on W diffuses from high to low temperature region establishing gradient of W in the opposite direction to gradient of T. Amplitude of W initially grows for ~0.1 ns and then fades away to 0 (as T profile flattens). The gradient of W creates an additional heat flux (see Eq.(2.2.13)) which is going against the heat flux created by T gradient. The relative amplitude of the 'counter flux' is limited to ~0.7 according to Figure 2.1 (according to the linear analysis the larger amplitude is possible (see Eq.(2.2.17)), e.g. ~0.999 for δ-functions description with S_i={9, 1.625, 6}, but it makes the numerical simulation unstable, possibly due to the nonlinear corrections at the points where $\left|\nabla K_T^{(2,L+1)} \cdot \nabla T\right|$ or $\left|\nabla K_W^{(2,L+1)} \cdot \nabla W\right|$ is larger or comparable to the linear flux divergence terms $\left|K_T^{(2,L+1)} \cdot \nabla^2 T\right|$ or $\left|K_W^{(2,L+1)} \cdot \nabla^2 W\right|$). The given above sets of values of S_i (parameters of the correction function $P_S(\xi)$) and L (determines the equation for W(x)) seem to provide the maximum possible value of the 'counter flux' for given functions P_S while keeping the simulation of the test problem stable.

2.3 Integral expression for the nonlocal heat flux across magnetic field

In the approach discussed in this Section we assume that the super-thermal electrons (which are responsible for the most of the heat flux) reach quasi-equilibrium within the space scale exceeding the mean free path much faster than thermal electrons do. Therefore if we are working on the timescale exceeding super-thermal electrons equilibration time (but less than the timescale of the thermal electrons equilibration) we can use quasi-steady state kinetic equation for the super-thermal electrons $\varepsilon / T >> 1$

$$\mathbf{v} \cdot \nabla f - (e\mathbf{E}/m) \cdot \nabla_{\mathbf{v}} f - \omega_{Be}[\mathbf{v} \times \mathbf{B}/B] \cdot \nabla_{\mathbf{v}} f = C_{ee} + C_{ei}, \qquad (2.3.1)$$

where the expressions for C_{ee} and C_{ei} were given in Section 2.2.1. Assuming **E**=-$\nabla\varphi$ we fuse two first terms on the left hand side of Eq.(2.3.1) into one by introducing a new variable $\varepsilon_T = mv^2/2 + e\varphi$ (e.i. in the potential field the distribution function is the function of total energy ε_{T}.)

$$\mathbf{v}\cdot\nabla f - \omega_{Be}\left[\mathbf{v}\times\mathbf{B}/B\right]\cdot\nabla_{\mathbf{v}} f = C_{ee} + C_{ei}\,. \tag{2.3.2}$$

To solve Eq.(2.3.2) we use the same approach as before and approximate f with a truncated spherical harmonics expansion $f(\mathbf{r},\mathbf{v}) = f_0(\mathbf{r},|\mathbf{v}|) + \mathbf{b}(\mathbf{r},|\mathbf{v}|)\cdot\mathbf{v}$ and take the 0^{th} and 1^{st} angular moments (multiply by 1 and **v**/|**v**|, and integrate over the full solid angle) of the Eq.(2.3.2) which provides us with two equations (where we neglected low order energy terms):

$$\nabla f_0 - \omega_{Be}\left[\mathbf{b}\times\mathbf{B}/B\right] = -\mathbf{b}/\tau_p\,, \tag{2.3.3}$$

$$\nabla\cdot\mathbf{b} = \frac{3}{Z}\frac{m}{\tau_p}\frac{\partial}{\partial\varepsilon}\left\{f_0 + T\frac{\partial f_0}{\partial\varepsilon}\right\}. \tag{2.3.4}$$

(Note that the electron-ion collisions wash out the anisotropic part of EDF (approximated as **b·v**) and the electron-electron collisions push the isotropic part of EDF towards Maxwellian EDF.) From the first of the equations we find the expression for **b**

$$\mathbf{b} = -\tau_p\nabla_{\parallel} f_0 - \tau_p\frac{\nabla_{\perp} f_0 - \tau_p\omega_{Be}\left[\mathbf{B}/B\times\nabla f_0\right]}{1+(\tau_p\omega_{Be})^2}, \tag{2.3.5}$$

and after the substitution into Eq.(2.3.4) we arrive at the following equation for f_0

$$\nabla\cdot\left\{-\tau_p\nabla_{\parallel} f_0 - \tau_p\frac{\nabla_{\perp} f_0 - \tau_p\omega_{Be}\left[\mathbf{B}/B\times\nabla f_0\right]}{1+(\tau_p\omega_{Be})^2}\right\} = \frac{3}{Z}\frac{m}{\tau_p}\frac{\partial}{\partial\varepsilon}\left\{f_0 + T\frac{\partial f_0}{\partial\varepsilon}\right\}. \tag{2.3.6}$$

To simplify the right hand side of Eq.(2.3.6) we introduce the new function [6] $\Psi = f_0 + T\partial f_0 / \partial\varepsilon$. We can rewrite it as $\Psi = \exp(-\varepsilon / T)\partial[\exp(\varepsilon / T) f_0] / \partial(\varepsilon / T)$ and find

$$f_0 = \exp\left(-\frac{\varepsilon}{T}\right)\left\{f_0(0) + \int_0^{\varepsilon}\Psi(\varepsilon')\exp\left(\frac{\varepsilon'}{T}\right)d\left(\frac{\varepsilon'}{T}\right)\right\}. \qquad (2.3.7)$$

If f_0 is not too far from the Maxwellian EDF $f_M = f_M(0)\exp(-\varepsilon / T)$ (which requires $\min(\lambda_{ei}, \rho_{Be}) < 1/k$) we can use $f_0 \approx f_M$ in the left-hand side of Eq.(2.3.6) to estimate the perturbation Ψ

$$\frac{1}{\varepsilon^{3/2}}\frac{\partial^2 f_M}{\partial x^2} \approx C_1 \frac{1}{\varepsilon^{3/2}}\frac{\partial\Psi}{\partial\varepsilon} . \qquad (2.3.8)$$

From Eq.(2.3.8) we find that $\Psi = \exp(-\varepsilon / T) \cdot P_5(\varepsilon)$, where $P_5(\varepsilon)$ is a 5th order polynomial. That allows us approximately to evaluate the integral in Eq.(2.3.7) to be $\Psi\exp(\varepsilon / T)\varepsilon / [6 \cdot T]$ using $(\varepsilon / T) > 1$, and, finally, find $\Psi \approx 6(f_0 - f_M)T / \varepsilon$. Note that $f_0(0) = f_M(0)$ because when $f_0 = f_M$ the function Ψ becomes zero. When calculating the derivative $\partial\Psi / \partial\varepsilon$ we can assume that multiplier T / ε is approximately constant ($(\varepsilon / T) > 1$) because f_0 and f_M vary exponentially

$$\frac{\partial}{\partial\varepsilon}\left\{f_0 + T\frac{\partial f_0}{\partial\varepsilon}\right\} \approx \frac{6T}{\varepsilon}\frac{\partial}{\partial\varepsilon}\{f_0 - f_M\}. \qquad (2.3.9)$$

Since f_0 is not too far from the Maxwellian EDF it provides a good approximation to the 'thermal' $\varepsilon / T \approx 1$ electron distribution as well which has only a minor contribution to the total electron heat flux (electrons with energy $\varepsilon / T < 3$ contribute <10% of the total heat flux for $f_0 = f_M$ and no magnetic field). This approximation allows us to use f_0 to describe EDF at *all* energies for the purpose of the heat flux calculation.

In the case when ∇T is in x-direction and **B** is in z-direction we obtain a diffusion-like equation for f_0 (the term [**B** x ∇f_0] drops out because its divergence is zero, since n, **B** and T are assumed to depend on x only)

$$-\frac{\partial}{\partial x}\left\{\frac{\tau_p}{1+(\tau_p\omega_{Be})^2}\frac{\partial f_0}{\partial x}\right\}=\frac{18m}{Z\tau_p}\frac{T}{\varepsilon}\frac{\partial}{\partial\varepsilon}\{f_0-f_M\}, \qquad (2.3.10)$$

with energy being the 'time' variable. Eq.(2.3.10) describes formation of the electron EDF by electrons coming from adjacent plasma while cascading from higher to lower energies. From Eq.(2.3.10) one can easily recover Eq.(2.1.1) describing the applicability of our nonlocal approach. Finally, using the Greens function of the diffusion equation in the WKB approximation we find from Eq.(2.3.10)

$$f_0(\varepsilon,\xi)=-\int_{\varepsilon}^{\infty}\int_{-\infty}^{+\infty}\frac{\exp\left\{-\dfrac{[\xi-\xi']^2}{4[D(\varepsilon)-D(\varepsilon')]}\right\}}{\sqrt{4\pi[D(\varepsilon)-D(\varepsilon')]}}\frac{\partial f_M}{\partial\varepsilon'}d\xi'd\varepsilon', \qquad (2.3.11)$$

where $d\xi=6\pi e^4\Lambda n\sqrt{5ZT}dx$, $D(\varepsilon)=5\int_{\varepsilon}^{\infty}p^4\left(1+S^3[p/T]^3\right)^{-1}dp$, and $S^3=16(\omega_{Be}\tau_{ei})^2/9\pi$. The expression for the particle and heat fluxes comes from the integral over the anisotropic part of the EDF, which gives:

$$\begin{bmatrix}j_x(x)\\ q_x(x)\end{bmatrix}=\int v_x\begin{bmatrix}1\\ mv^2/2\end{bmatrix}f(x,\mathbf{v})d\mathbf{v}=-\frac{8\pi\sqrt{2}}{3m^{5/2}}\int_0^{\infty}\begin{bmatrix}\varepsilon^{3/2}\\ \varepsilon^{5/2}\end{bmatrix}\frac{\tau_p}{1+(\tau_p\omega_{Be})^2}\frac{\partial f_0}{\partial x}d\varepsilon. \qquad (2.3.12)$$

In Eq.(2.3.12), the x-derivative $\partial f_0/\partial x$ is calculated from Eq.(2.3.11), after which we can switch the derivative variable from x to –x', and then integrate by parts the product of the Green's function [which depends on both x and x' through ξ and ξ'] by $\partial f_M/\partial\varepsilon'$ [which depends only on $\xi'(x')$]. After the substitution of Eq.(2.3.11) into Eq.(2.3.12) we get

$$\begin{bmatrix} j_x(x) \\ q_x(x) \end{bmatrix} = -\int_{-\infty}^{\infty} \left\{ \begin{bmatrix} P_1(x,x') \\ P_2(x,x') \end{bmatrix} \frac{\partial T}{\partial x'} - \begin{bmatrix} P_3(x,x') \\ P_4(x,x') \end{bmatrix} \frac{\partial e\varphi_{nl}}{\partial x'} \right\} dx', \qquad (2.3.13)$$

where $e\varphi = e\varphi_l + e\varphi_{nl}$; $e\varphi_l = T(d\ln n/dx - (5/2)d\ln T/dx)$ is the electrostatic potential energy in a <u>local</u> equilibrium and $e\varphi_{nl}$ is a correction due to nonlocal effects [12]; $P_i(x,x')$ are the appropriate kernels derived from Eq.(2.3.12)

$$\begin{bmatrix} P_1 & P_3 \\ P_2 & P_4 \end{bmatrix} = \frac{2\sqrt{10}n}{\pi\sqrt{Zm}} \int_0^{\infty} \int_{\varepsilon}^{+\infty} \frac{\exp\left\{ -\frac{[\xi-\xi']^2}{4[D(\varepsilon)-D(\varepsilon')]} - \frac{\varepsilon'}{T} \right\}}{\sqrt{D(\varepsilon)-D(\varepsilon')}} \begin{bmatrix} \varepsilon'/T & 1 \\ (\varepsilon'/T)\varepsilon & \varepsilon \end{bmatrix} d\varepsilon' \frac{(\varepsilon/T)^3}{1+S^3(\varepsilon/T)^3} d\varepsilon. \qquad (2.3.14)$$

We can proceed further by setting the electron current j_x to zero, which gives us the integral equation for the nonlocal electric field, which enters the expression for the nonlocal heat flux. However, the solution is expected to be very cumbersome, and for practical usage we can try to simplify Eq.(2.3.13). One of the possible ways is to approximate the heat flux $q_x(x)$ only with the first term under integral in Eq.(2.3.13) and account for the electric field effects through the normalization against the Fokker-Plank simulation. This assumption is justified if we would be able to closely reproduce FP results in a wide range of $k\lambda_{ei}$ ($0.01 < k\lambda_{ei} < 1$) with only two normalization constants. We would need a second constant to account for the B-field impact on the nonlocal E-field. With this simplification we obtain the following expression for the nonlocal heat flux

$$q_x(x) = -\sqrt{\frac{2T}{m}} \int_{-\infty}^{+\infty} n \frac{\partial T}{\partial x'} P(x,x') dx', \qquad (2.3.15)$$

where

$$P(x,x') = \frac{4C_A G}{\pi\sqrt{5Z}} \int_0^{\infty} u \exp(-u) \left\{ \sqrt{\rho}\exp(-1/\rho) + \sqrt{\pi}\left(\mathrm{erf}(1/\sqrt{\rho}) - 1\right) \right\} du, \qquad (2.3.16)$$

$$\rho \equiv \rho(u, S_B, G) = \frac{5}{S_B^5 G^2}\left\{\frac{t^2}{2} + \frac{1}{3}\ln\frac{1+t}{\sqrt{t^2 - t + 1}} - \frac{1}{\sqrt{3}}\left[\frac{\pi}{6} + a\tan\frac{2t-1}{\sqrt{3}}\right]\right\}_{t = uS_B},$$

$$G \equiv G(x, x') = \frac{3\pi e^4\sqrt{5Z}}{T(x')^{5/2}}\int_{x'}^{x} n(x'')\Lambda(x'')\sqrt{T(x'')}dx'',$$

$$S_B^3 = 16C_B^2(\omega_{Be}\tau_{ei})^2/9\pi.$$

The kernel P given in Eq.(2.3.16) has been simplified by calculating the integral over ε and it is a function of only two parameters P = P(G,S_B). Therefore, P is a constant surface in the space of the parameters $\omega_B\tau_{ei}$ and G which can be interpreted as the effective magnetic field and distance correspondingly. Constants $C_A < 1$ and C_B are introduced to account for the neglected ambipolar electric field, where C_A accounts for the impact of the nonlocal E-field and C_B accounts for the change in the nonlocal E-field due to B-field. In general C_A and C_B are the functions of $k\lambda_{ei}$ but we expect these functions to be weak enough to allow the approximation with a constant in the wide range of $k\lambda_{ei}$ values.

We applied the expression for nonlocal heat flux given in Eq.(2.3.15-16) to the test problem described in Section 2.2.3. In that problem <T> grows linearly with time (constant heating and no losses) from T(t=0) = 1keV to T(t=0.5ns) = 3.2keV, and, therefore, (for given constant B-field) the average magnetization $\omega_B\tau_{ei} \sim \langle T\rangle^{3/2}$ increases 6 times from its initial value at T(t=0). We calculated a set of relative temperature peak $(T_{max}-T_{min})/\langle T\rangle$ curves for different values of B-field. The values of the magnetic field were chosen in a way that at temperature T(t=0) the values of $\omega_B\tau_{ei}$ would be 0, 0.1, and 1. The time evolution of the 'non-locality' parameter $k\lambda_{ei}/(1+\omega_B^2\tau_{ei}^2)$ with and without a magnetic field is shown on the Figure 2.2. We tested our model against the Fokker-

Planck (FP) simulation data obtained by using the IMPACT code [8] which also uses Lorentz approximation. The best fit to the FP simulation for $\omega_B\tau_{ei} \in [0; 6]$ and $k\lambda_{ei} \in [0.06; 0.6]$ was achieved with C_A=0.11 and $C_B^2 = 0.34$ (see Figure 2.5).

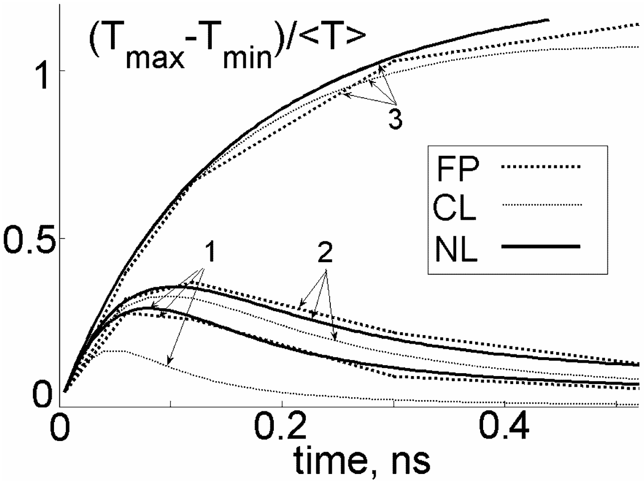

Figure 2.5 Time evolution of (T_{max}-T_{min})/<T> according to classical [10] (Epperline) theory ('CL' curve), nonlocal model ('NL' curve with C_A=0.11 and $C_B^2 = 0.34$) and the results from the IMPACT kinetic code [8] ('FP' curve) for different initial values of magnetization $\omega_B\tau_{ei}$ (0 corresponds to curve '1'; 0.1 to curve '2'; 1 to curve '3').

These values of the constants are not too far from the values one would get by matching the classical [24] heat flux model in the limit $k\lambda_{ei}$ << 0.01 at $\omega_B\tau_{ei}$<<1 and $\omega_B\tau_{ei}$ >> 1 ($C_A^* = 0.167$ and $(C_B^*)^2 = 0.154$). The value of C_A (the heat flux multiplier) corresponding to larger $k\lambda_{ei}$ is somewhat smaller (than C_A^*) accounting for the presence of the additional nonlocal E-field (dropped out in Eq.(2.3.15) which is the simplification of Eq.(2.3.13)) inhibiting the heat flux. The value of $(C_B^*)^2$ (the magnetic field multiplier) is less than C_B^2 because the contribution from the additional E-field gets smaller as $\omega_B\lambda_{ei}$

increases. By slightly adjusting only 2 constants in our model we were able to closely reproduce 3 nontrivial curves (see Figure 2.5, for $(\omega_B \tau_{ei})_{t=0}$ = 0, 0.1, 1; and $k\lambda_{ei} \in [0.06; 0.6]$) from the FP simulation [8]. We recommend using this model with $C_A = 0.11$ and $C_B^2 = 0.34$ in simulations including magnetic field where $k\lambda_{ei} \gtrsim$ 0.01. We are not aware of any other works which provide the analytical treatment of nonlocal heat transport across B-field for strong temperature variations.

2.4. Conclusions

In this work we considered two different ways to improve the accuracy of the heat flux calculations based on the hydrodynamic model in the limit of weak collisionality. In the first approach the addition of a one scalar moment of EDF to the set of classical hydro moments increases the maximum value of $k\lambda_{ei}$ in the applicability range by 30. The linear decay rate provided by the presented model is in a good agreement with kinetic simulation results up to $k\lambda_{ei} \lesssim 0.3$ as oppose to $k\lambda_{ei} \lesssim 0.01$ for the classical model (see Figure 2.1). This approach given by Eq.(2.2.12) provides rather straightforward (compared to delocalized models) and more rigorous (compared to flux limiters) way to account for the effect of the collisionless tail of EDF on the heat transport for $k\lambda_{ei} \lesssim 0.3$. For $k\lambda_{ei} \gtrsim 0.3$ the model reduces to the regular hydro model with a flux limiter set to 0.3. For the cases when $k\lambda_{ei}$ can exceed 0.3 (or when the magnetic field is important) we consider another approach to the heat flux.

In the second approach we find the equilibrium distribution of hot electrons in the presence of B-field and obtain the expression for the heat flux containing unknown nonlocal E-field. Assuming that the relative contribution from the nonlocal E-field to the heat flux is approximately constant over a wide range of $k\lambda_{ei}$ values (but allowing it to vary with B-field imposed) we neglect the ambipolar field term, but include two normalization constants (whose values are defined against Fokker-Planck simulations) that account for the electric field effects and the B-field impact on the non-local E-field. The corresponding expression for the heat flux across B-field given in Eq. (2.3.15-16) is applicable as long as $\min(\lambda_{ei}, \rho_{Be}) < 1/k$ and reproduce the Fokker-Planck simulation results quite well in a wide range of parameters. Overall this approach provides a way to account for the nonlocal heat transport across magnetic field in hydrocodes even when the perturbation approach [20] is not applicable.

2.5 Acknowledgement

The text of this chapter, in full, includes material from “Heat flux calculation in the semi-collisionless regime for substantial temperature variations including magnetic field” [B.K. Frolov, S.I. Krasheninnikov, R.J. Kingham and J. Edwards, New J. Phys. **8**, 56 (2006)]. The dissertation author was the primary researcher.

2.6 Bibliography

[1] D. Strickland and G. Mourou, *Opt. Commun.* **56,** 219 (1985)

[2] M. Tabak, J. Hammer, M. E. Glisky, W. L. Kruer, W. C. Wilks, and R. J. Mason, *Phys. Plasmas* **1,** 1626 (1994)

[3] J. Lindl, *Phys. Plasmas* **2,** 3933 (1995)

[4] J. Villasenor and O. Buneman, *Comp. Phys. Comm.* **69,** 306 (1992)

[5] J. Dawson, *Rev. Mod. Phys.* **55** 403, (1983)

[6] C. K. Birdsall and A. B. Langdon, *Plasma Physics via Computer Simulations* (New York: Adam Hilger) (1991)

[7] R. W. Hockney and J. W. Eastwood, *Computer Simulation Using Particles* 540 S (London: McGraw Hill) (1981)

[8] R. J. Kingham and A. R. Bell, *J. Comput. Phys* **194,** 1 (2004)

[9] L. Spitzer and H. Harm, *Phys. Rev.* **89,** 977 (1953)

[10] E. M. Epperlein and M .G. Haines, *Phys. Fluids* **29,** 1029 (1986)

[11] D. G. Colombant, W. M. Manheimer, and M. Busquet, *Phys. Plasmas* **12,** 072702 (2005)

[12] J. R. Albritton, E. A. Williams, and I. B. Berstein, *Phys. Rev. Lett.* **57,** 1887 (1986)

[13] S. I. Krasheninnikov, *Phys. Fluids B* **5,** 74 (1993)

[14] R. J. Kingham and A. R. Bell, *J. Comput. Phys* **194,** 1 (2004)

[15] H. Grad, *Commun Pure Appl. Math.* **2,** 325 (1949)

[16] H. Grad, *Principles of the kinetic theory of gases*, in *Handbuch der Physik*, edited by S. Flugge (Berlin: Springer), Vol. 12. (1958)

[17] H. Struchtrup, M. Torrilhon, *Phys. Fluids* **15**, 2671 (2003)

[18] T. K. Kho and D. J. Bond, *J. Phys. D.* **14,** L117 (1981)

[19] D. J. Bond, *J. Phys. D.* **14,** L43 (1981)

[20] A. V. Brantov, V. Yu. Bychenkov, W. Rozmus, C. E. Capjack and R. Sydora, *Phys. Plasmas* **10,** 4633 (2003); Z. Chang and J. D. Callen, *Phys. Fluids B* **4**, 1167 (1992); V. P. Silin, JETP **79**, 236 (1994); K. Yu. Vagin and V. P. Silin, *Plasma Phys. Rep.* **24**, 750 (1998).

[21] A. Tahraoui and A. Bendib, *Phys. Plasmas* **9,** 3089 (2002)

[22] G. P. Schurtz, Ph. D. Nicolai and M. Busquet, *Phys. Plasmas* **7,** 4238 (2000)

[23] V. P. Silin, *Physics-Uspekhi* **45,** 955 (2002)

[24] S. I. Braginskii, *Transport Processes in a Plasma,* in Review of Plasma Physics, Leontovich M A (ed.), New York: Consultants Bureau, Vol.1 (1965)

[25] P. Nicolai, M. Vandenboomgaerde, B. Canaud and F. Chaigneau, *Phys. Plasmas* **7,** 4250 (2000)

[26] E. M. Epperlein, *Phys. Rev. Lett.* **65,** 2145 (1990)

3

Beam Propagation in Solid Insulators

3.1 Introduction

A high energy electron beam is generated when a high intensity laser pulse interacts with matter. As a result of the interaction of this beam with a thin foil an energetic proton beam can be produced [1-4] which can be utilized in many applications ranging from the Fast Ignition scheme of the Inertial Confinement Fusion [5] to medicine [6]. The quality of the proton beam (characterized by beam emittance and energy spread) is determined by the electron beam quality which can be affected by the foil material as well as other parameters. The material of the foil is important because the propagation of an intense electron beam through the initially cold matter of the foil is influenced by the collisional and field ionization (where the E-field pulls electrons and ions apart) processes. The latter is especially important in insulators.

The dynamics of the laser-generated electron beam and the associated ionization front were studied in a number of works [7-14]. In experiments [9] glass targets were used to observe the time and space evolution of the fast electron beam propagating through a solid target. Two distinct types of fast electron propagation in a glass target were reported: a collisional electron cloud expansion accompanied by a highly collimated electron jet. In Reference [11] it was shown that the jet observed in the experiment [9] could be explained by the presence of field ionization causing filamentation type instability. This instability has been previously observed in a number of experiments [8,12] when a dielectric target was used. The use of a metal target in the same experiments [8,12] produced no sign of the instability. In this Chapter we study in detail the impact of field ionization on the electron beam propagation in solid density insulators, continuing the line of analysis started in [11]. We show the reasons behind the non-monotonic front velocity dependence on the beam density. We also show the dependence of the front velocity on the steepness of the incoming beam density profile and discuss the impact of the polarization current induced by field ionization.

An electron beam (with density n_b) propagating through a medium with a small free electron density $n_e<n_b$ (initial atom density $n_0 > n_b$) has to ionize the medium up to electron densities n_e greater than n_b in order to sustain the balancing return current. The corresponding ionization front moves at the speed V_f which is determined by the total ionization rate of collisional and field ionization processes.

The characteristic time and space scale of the ionization front dynamics can be estimated as follows. The velocity of the return current electrons behind the ionization front is equal to the beam current $V_f n_b$ divided by the free electron density. The possible electron density cannot exceed the atom density n_0 (assuming a single ionization), and, therefore, the return current drift velocity does not decrease below $V_f n_b / n_0$. This allows us to find the residual E-field behind the wave by using the drift velocity $V_E \approx eE/(m\nu_e)$

$$E_{res} = \frac{mV_f \nu_e}{e} \frac{n_b}{n_0}, \tag{3.1.1}$$

where $\nu_e = \max(\nu_{ea}, \nu_{ei})$; ν_{ea} and ν_{ei} are the electron-atom and electron-ion collision frequencies; e and m are the electron charge and mass. The amplitude of E_{res} does not exceed a few percent of the atomic E-field, $E_a \approx 10^9\,V/cm$, because a strong E-field would entail the full ionization of the medium and the strong acceleration of the return current (T>100eV), resulting in a low collision frequency. We can neglect E_{res} as long as the associated change in the potential is small compared to W_b, i.e. the front separation from the beam source is much less than $W_b/(eE_{res})$, where W_b is the maximum beam electron energy in the front frame. For $n_b = 10^{18}\,cm^{-3}$ we have $E_{res} \approx 3 \cdot 10^6\ V/cm$, and $W_b/(eE_{res}) \approx 300\,\mu m$ for W_b~100 keV. The thickness of the wave can be estimated as $W_b/(eE_a) \approx 1\,\mu m$ for W_b = 100 keV. The time required to establish the steady state front propagation is approximately $W_b/(ceE_a) \approx 10^{-14}$ s. The model derived below is applicable as long as the time and the space allowed exceed these values.

Note that the beam density n_b has to include only the beam electrons moving faster than the ionization front. Imagine observing from the reference frame which moves with the velocity V_f of the ionization front. The beam electrons with laboratory frame velocities below V_f cannot keep up with the front. Therefore, the beam density n_b in this moving frame has to be redefined as the density of beam electrons whose laboratory frame velocities exceed V_f. The moving frame beam density can be order of magnitude smaller than original beam density depending on the beam energy W_b and the ionization front velocity V_f.

In this work we use the 1D approximation to describe the ionization front, and, therefore, the beam current density and the return current density are laterally uniform. Assuming a steady front propagation, these currents have to exactly cancel each other, thus, generating no B-field. Corrections due to a non-uniform current distribution and different instabilities (e.g. two-stream instability) are not included in this treatment.

3.2. Derivation of ionization front velocity using quasi-neutral region

If the ionization front steadily propagates with the velocity V_f (which remains to be determined) then in the front rest frame we have the following continuity equations for ions and electrons:

$$\nabla \cdot (\mathbf{V}_f n_i) = \nu_{EI}(\mathbf{E}) N_a + \nu_{bI} n_b + \nu_{eI} n_e , \qquad (3.2.1)$$

$$\nabla \cdot \left\{ (\mathbf{V}_f + \mathbf{V}_{E_a} \varepsilon) n_e \right\} = \nu_{EI}(\mathbf{E}) N_a + \nu_{bI} n_b + \nu_{eI} n_e , \qquad (3.2.2)$$

where $V_{Ea} = eE_a / (\gamma_f m \nu_e)$ is the electron drift velocity (in the ionization front frame moving with velocity $V_f >> V_{Ea} \varepsilon$) caused by the E-field with amplitude -E_a; $\varepsilon = -E / E_a$ is the dimensionless E-field (where $E_a = (2/3)(I_a / I_H)^{5/2} e / a_B^2$, I_a is the ionization potential of the atom, I_H is the hydrogen ionization potential, a_B is the Bohr radius); $\gamma_f = 1/(1 - V_f^2 / c^2)^{1/2}$; ν_{bI} and ν_{eI} are the ionization frequencies for collisions with the beam and secondary electrons respectively (we assume $\nu_{bI} = K_{bI} N_a$ and $\nu_{eI} = K_{eI} N_a$, where K_{bI} and K_{eI} are constants); ν_{EI} is the field ionization frequency; N_a is the density of atoms in the insulator, $N_a(x) \leq n_0$. Subtracting these two equations we find an expression for the field induced charge separation:

$$(n_i - n_e) \approx n_i \varepsilon \cdot V_{Ea} / V_f \,. \tag{3.2.3}$$

At the back of the ionization front (where the E-field has to vanish because a nonzero field in 1D can exist only inside of the front) we can assume the quasi-neutrality condition (i.e. the difference between the beam density n_b and the induced charge density $(n_i - n_e)$ is relatively small) to find the amplitude of the E-field there. We also assume that the beam density is shaped according to a power law, $n_b = \overline{n}_b \phi^p$, where ϕ is the normalized potential, $\phi = e\varphi / W_b$. ϕ=0 at the head of the beam and ϕ=1 at the back of the beam; W_b is the maximum value of the beam electron energy (in the ionization front reference frame). The parameter p allows us to introduce the steepness of the beam profile into the equations. Using Eq.(3.2.3) and the beam density profile $n_b = \overline{n}_b \phi^p$ we find that the normalized E-field at the rear of the ionization front is

$$\varepsilon = \frac{\overline{n}_b \phi^p V_f}{n_i(x) V_{Ea}} \,. \tag{3.2.4}$$

In 1D geometry the E-field can be written as the gradient of the potential,

$$\varepsilon = d\phi / dx \cdot (W_b / eE_a) \,, \tag{3.2.5}$$

therefore, we can integrate Eq.(3.2.4) over the quasi-neutral region at the back of the beam stretching from $x=x_1$ (which remains to be determined) to $x=-\infty$ (for the beam going in the positive x direction (see Figure 3.1), or in terms of potential, from $\phi = \phi_1$ to ϕ=1) to find the ionization front velocity V_f as a function of unknown x_1 (or ϕ_1).

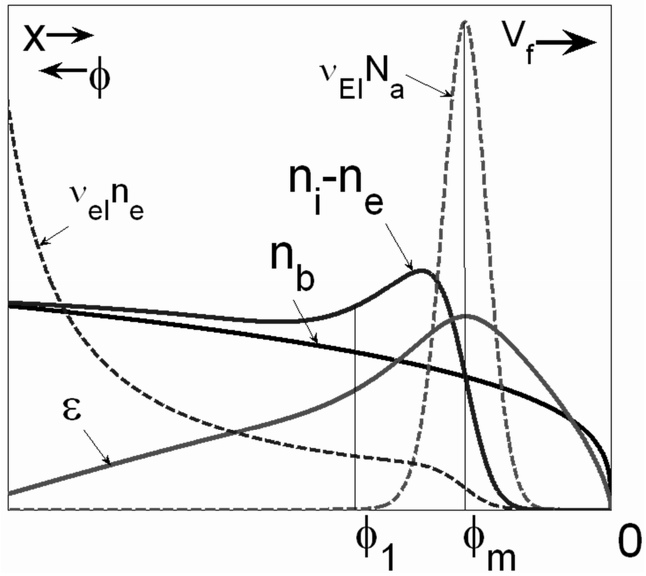

Figure 3.1. The qualitative structure of the E-field, beam and induced charge densities, and ionization rates for the case $\phi_m^{\max Vf} < \phi_m < 1$ ($n_b = 10^{18}\,\mathrm{cm}^{-3}, n_0 = 3\cdot 10^{22}\,\mathrm{cm}^{-3}$, p=0.3).

We find the function $n_i(x)$ in this region by exploiting the fact that collisional ionization dominates, and, therefore, the continuity equation for ions Eq.(3.2.1) simplifies to

$$V_f dn_i / dx \approx \nu_{eI} n_i . \tag{3.2.6}$$

Hence,

$$n_i = n_i(x_1)\exp\left(\frac{\nu_{eI}}{V_f}\left[x - x_1\right]\right). \tag{3.2.7}$$

After the substitution of Eq.(3.2.7) into Eq.(3.2.4) and the subsequent integration we obtain the ionization front velocity as a function of two unknowns: the potential ϕ_1 and the ion density $n_i(x_1) \equiv n_i(\phi_1)$ at the beginning of the quasi-neutral region

$$V_f^2 = \frac{1-\phi_1^{1-p}}{1-p}\frac{n_i(\phi_1)}{\bar{n}_b}\frac{W_b\nu_{eI}}{eE_a}V_{Ea} . \tag{3.2.8}$$

We find it is more convenient to use the dimensionless electrostatic potential $\phi = e\varphi / W_b$, $0 \le \phi \le 1$, as the variable instead of the space coordinate x, $-\infty < x \le x(\phi = 0)$.

The value of x as a function of ϕ is given by the following equation which is derived from Eq.(3.2.5)

$$x(\phi) = x(\phi = 0) + \frac{W_b}{eE_a} \int_0^{\phi} \frac{d\phi'}{\varepsilon(\phi')} . \tag{3.2.9}$$

3.3 Non-neutral region impact on the ionization front velocity

The potential ϕ_1 and the ion density $n_i(\phi_1)$ are determined by the preceding strongly non-neutral region where the beam charge causes the E-field to grow. The potential ϕ_m ($\phi_1 > \phi_m$) corresponding to the maximum value of the E-field can be estimated from Poisson's equation, $dE/dx = -4\pi e\left(\bar{n}_b \phi^p - (n_i - n_e)\right)$, applied at the beam head (where the contribution from n_i-n_e is small)

$$\phi_m = \left[\frac{E_a^2 (p+1)}{8\pi W_b \bar{n}_b} \varepsilon_m^2 \right]^{\frac{1}{p+1}} , \tag{3.3.1}$$

where we used Eq.(3.2.5). The maximum value of the E-field, ε_m, can be found from the equation derived in [Ref.[11], Eq.(29)]. (Later in this Chapter we return to and derive the more general expression for ε_m including the polarization current.)

$$\varepsilon_m^3 \nu_{EI}(\varepsilon_m) = \frac{8\bar{n}_b^2 \phi_m^{2p} V_f^2 e}{E_a V_{E_a} N_a} , \tag{3.3.2}$$

where $\nu_{EI}(\varepsilon_m) = \nu_a e^{-1/\varepsilon_m} / \varepsilon_m$; $\nu_a = 6me^4 / \hbar^3$; $\hbar$ is the Planck constant. From Eq.(3.3.2) we find that $\varepsilon_m << 1$ due to the exponential dependence of $\nu_{EI}(\varepsilon_m)$ on ε_m, which also entails a very weak logarithmic dependence of ε_m itself on other parameters.

Depending on the value of ϕ_m (and using Eq.(3.3.1)) the ionization front structure can be described by one of the three following cases. In the first case $\phi_m \approx 1$ (the beam density $\bar{n}_b$ is very small ($W_b \bar{n}_b \approx \varepsilon_m^2 E_a^2 / 8\pi$)). The quasi-neutral approximation is not good for $\phi > \phi_m$ because the value of the E-field changes from ε_m to 0 within the small potential range $1-\phi_m$ which requires the total space charge density there to be greater than $\bar{n}_b$. This case is not very interesting due to the small beam density and the correspondingly small field amplitude.

In the second case $\phi_m < 1$ ($W_b \bar{n}_b > \varepsilon_m^2 E_a^2 / 8\pi$). The peak E-field moves closer to the beam head (see Figure 3.1) due to fast charge neutralization enabled by field ionization (within the non-neutral region) caused by the strong E-field. The total ion density produced by field ionization is approximately $2n_i(\phi_m)$ due to the symmetry of the E-field profile near its maximum value. Therefore, $n_i(\phi_1) \approx 2n_i(\phi_m)$, and we can use $\phi_1 \approx \phi_m$ because the relative width of the field ionization region is small, i.e. $\delta\phi_m / \phi_m = \varepsilon_m / (2(p+1)\sqrt{\pi}) << 1$ (which is derived by expanding ε near ε_m and integrating $V_f dn_i / dx \approx \nu_{EI}(\varepsilon) n_0$ from 0 to ϕ_m). Substituting $n_i(\phi_m)$ from Eq.(3.2.4) (at the point ϕ_m the quasi-neutrality condition is also satisfied) yields

$$V_f \approx \frac{1-\phi_m^{1-p}}{1-p} \frac{\phi_m^p}{\varepsilon_m} \frac{2W_b \nu_{eI}}{eE_a} . \tag{3.3.3}$$

The front velocity has its maximum value when ϕ_m is equal to $\phi_m^{\max V_f} \approx p^{1/(1-p)}$ and the corresponding beam density can be found from Eq.(3.3.1). The velocity V_f grows with the beam density up to $V_f(\phi_m^{\max V_f})$ and than starts falling proportional to a small negative power -p/(p+1) of $\bar{n}_b$ (see Figure 3.2).

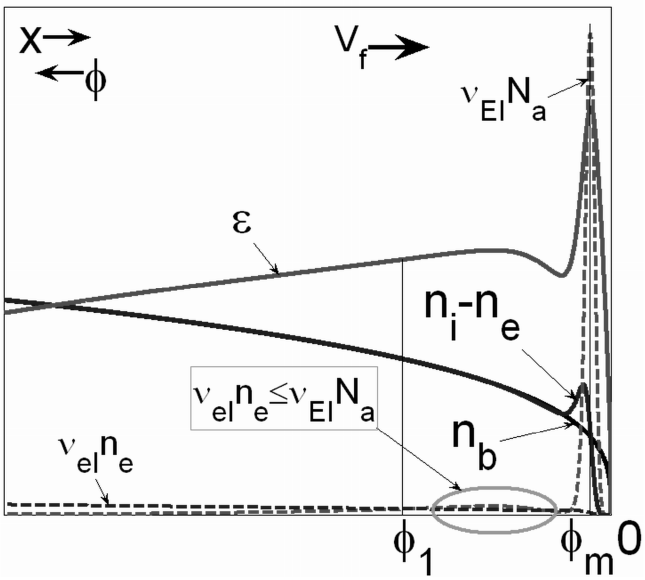

Figure 3.2 The structure of the E-field, beam and induced charge densities, and ionization rates for the case $\phi_m < \phi_m^{\max V_f}$ ($n_b = 10^{20}\,\mathrm{cm}^{-3}, n_0 = 3\cdot 10^{22}\,\mathrm{cm}^{-3}$, p=0.3). The green ellipse shows the new region (compared to Figure 3.1) where the quasi-neutrality condition is satisfied and field ionization is dominant.

In the third case $\phi_m \ll 1$ ($\phi_m < \phi_m^{\max V_f}, W_b \bar{n}_b \gg E_a^2/8\pi$). The E-field is so strong that field ionization becomes dominant within some part of the quasi-neutral region (see Figure 3.3). Consider this part of the quasi-neutral region to be a separate region connecting the non-neutral region and the collision ionization dominated part of the quasi-neutral region. In this case the values of ϕ_1 and $n_i(\phi_1)$ required for Eq.(3.2.8) are determined by *field ionization* (not collisional ionization as it was before), i.e. $V_f dn_i / dx \approx \nu_{EI}(\varepsilon) n_0$.

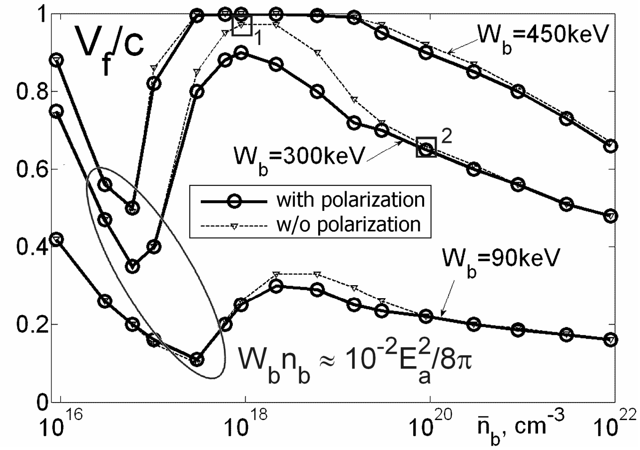

Figure 3.3 The velocity of the ionization front is given as a function of electron beam density $\bar{n}_b$ ($n_b = \bar{n}_b \phi^p$) for different beam electron energies measured in the reference frame of the front. The dotted lines with triangles correspond to the front velocity calculated neglecting the polarization current. Squares with numbers 1 and 2 refer to beam densities for which Figure 3.1 and Figure 3.3 are plotted, correspondingly.

Substituting n_i from Eq.(3.2.4) (which is derived from the quasi-neutrality condition) and using the relationship $d/dx = \varepsilon e E_a / W_b \cdot d/d\phi$, we obtain the equation for the E-field in this new region:

$$\frac{\varepsilon \nu_{EI}(\varepsilon)}{p\frac{\varepsilon}{\phi} - \frac{\partial \varepsilon}{\partial \phi}} = \frac{eE_a}{W_b} \frac{\bar{n}_b \phi^p V_f^2}{n_0 V_{E_a}}, \qquad (3.3.4)$$

or

$$\varepsilon = \frac{1}{\ln A_1}, \qquad (3.3.5)$$

where

$$A_1 \equiv \frac{W_b \nu_a}{eE_a} \frac{n_0 V_{E_a}}{\bar{n}_b \phi^p V_f^2} \left[p \frac{\varepsilon}{\phi} - \frac{\partial \varepsilon}{\partial \phi} \right]^{-1}. \tag{3.3.6}$$

When $\phi_m << 1$ the potential ϕ_1 ($\phi_1 >> \phi_m$), which is defined as the beginning of the quasi-neutral *and* collision ionization dominated region, corresponds to the point where the value of the field ionization rate drops below the collisional ionization rate $\nu_{EI}(\phi_1) N_a \approx \nu_{eI} n_i(\phi_1)$. To find $\varepsilon(\phi_1)$ from this expression we use Eq.(3.3.4) to eliminate $\nu_{EI}(\phi_1)$ which yields

$$\varepsilon(\phi_1) \approx \frac{N_a}{n_i(\phi_1) A_1(\phi_1)} \frac{\nu_a}{\nu_{eI}}, \tag{3.3.7}$$

where we also used Eq.(3.3.5). Combining Eq.(3.3.7) with the quasi-neutrality condition given by Eq. (3.2.4) we find

$$\phi_1 \approx \frac{eE_a p}{W_b \nu_{eI}} V_f \varepsilon(\phi_1). \tag{3.3.8}$$

Now we substitute $n_i(\phi_1)$ from Eq.(3.2.4) (where we use $\varepsilon(\phi_1)$ from Eq.(3.3.5)) into the expression for V_f given in Eq.(3.2.8) and find that for $\phi_m << 1$

$$V_f \approx \frac{1-\phi_1^{1-p}}{1-p} \frac{\phi_1^p}{\varepsilon(\phi_1)} \frac{W_b \nu_{eI}}{eE_a}. \tag{3.3.9}$$

Finally, by substituting Eq.(3.3.9) into Eq.(3.3.8) we obtain an equation for ϕ_1 which immediately yields that ϕ_1 is a constant:

$$\phi_1 = p^{1/(1-p)}. \tag{3.3.10}$$

Therefore V_f exhibits only weak logarithmic dependence on $\bar{n}_b$ through ε (see Eq.(3.3.9)). Eq.(3.3.10) also implies that at high beam densities the change in the normalized potential (1-ϕ_1) within the collisional ionization region inside the quasi-neutral region is fixed. Whereas the potential ϕ_m corresponding to the maximum E-field steadily falls with the beam density according to Eq.(3.3.1), since ε_m is almost a constant. That leaves increasingly more space (from ϕ_m to ϕ_1) for the field ionization dominated quasi-neutral region which can be seen on Figure 3.3. Note: if V_f approaches speed of light then the value of A_1 in Eq. (3.3.5) becomes very small due to the γ_f factor in the characteristic drift velocity V_{Ea}. This increases $\varepsilon(\phi_1)$ and forces V_f to decrease to keep $V_f \cdot \varepsilon(\phi_1) = \text{constant}$ (which follows from Eq. (3.3.8)). Finally, Figure 3.4 illustrates how the front velocity depends on the beam density $n_L = n_b / \sqrt{1 - c_f^2}$ and energy $W_L / mc^2 = (1 + c_f c_b) / \sqrt{(1 - c_f^2)(1 - c_b^2)} - 1$ in the laboratory frame, where $c_f = V_f/c$ and $c_b = \sqrt{1 - (1 + W_b / mc^2)^{-2}}$.

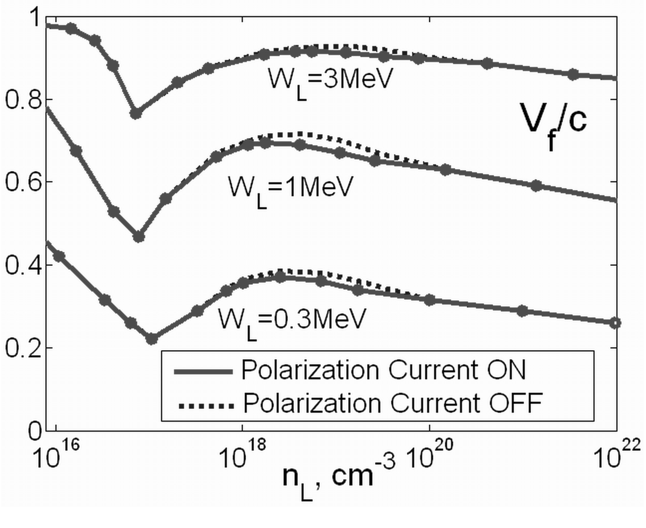

Figure 3.4. The ionization front velocity is plotted vs. beam density n_L (p=0.3) in the laboratory frame for three different beam energy W_L values in the laboratory frame 0.3 MeV, 1 MeV, and 3 MeV. The values of the velocity are obtained from numerical solution of Eq. (12, 13) from [11] with and without addition of the polarization current.

Before considering the effects of the polarization current (caused by the field ionization charge separation) on the ionization front structure and its speed let us summarize the findings. If we start at low beam densities and move to higher beam densities the ionization front speed initially decreases due to the decrease in the beam Debye length. When the beam energy density becomes comparable to about 1% of the energy density of an atomic E-field (which corresponds to ϕ_m being substantially less than 1), field ionization becomes important and helps to accelerate the front by increasing the effective ionization rate. The additional electrons created by field ionization serve as a seed for further collisional ionization. The E-field causes electrons to move to the rear of the beam creating a return current. This current creates an uncompensated positive charge of unmovable ions resulting in reduction of the E-field amplitude along the beam. (Note that for a smooth beam head density profile, $n_b = \bar{n}_b \phi^p$ ($0<p<1$), the strong E-field vanishes before the beam density n_b fully develops into $\bar{n}_b$.) The higher the beam density $\bar{n}_b$ the earlier the E-field "cut–off" occurs (due to the increasing number of electrons generated by the field ionization), resulting in the reduction of the field ionization contribution and the deceleration of the ionization front. For even higher beam densities ($\phi_m \ll 1$) the field ionization rate <u>after</u> the cut-off becomes comparable to the collisional ionization rate, and the velocity decline with the beam density becomes logarithmically weak.

3.4 Polarization current effects

In our analysis of the ionization front so far we have neglected the current induced by the field ionization itself. This current can inhibit the strong field formation and therefore may be worth considering. The amplitude of the current, j_{polar} (with the dimensionality of particle flux), can be derived from the balance of the work done by the E-field, $-ej_{polar}E$, and the energy input required by the field ionization, $I\nu_{EI}N_a$,

$$j_{polar} = -\frac{I\nu_{EI}N_a}{eE_a\varepsilon}, \tag{3.4.1}$$

where I is the ionization energy. This field ionization induced current will have the largest amplitude at the point ϕ_m of maximum field strength ε_m. The new equation (modified Eq.(3.2.4)) for E-field ε_m is

$$\bar{n}_b\phi_m^p V_f = n_i(\phi_m)V_{Ea}\varepsilon_m + j_{polar}(\phi_m) \tag{3.4.2}$$

The new expression for $n_i(\phi_m)$ can be found by expanding ε near ε_m and integrating $V_f dn_i/dx \approx \nu_{EI}(\varepsilon)N_a$ from 0 to ϕ_m:

$$n_i(\phi_m) = \sqrt{\frac{E_aN_a}{8V_{Ea}e}\varepsilon_m\nu_{EI}(\varepsilon_m)}\,. \tag{3.4.3}$$

Solving Eq.(3.4.2) for $\nu_{EI}(\varepsilon_m)$ we find

$$\sqrt{e^{1/\xi_m}} = \sqrt{\frac{n_0}{\bar{n}_b}\frac{\nu_a I}{eE_aV_f}\frac{1}{\phi_m^pA_2}}\left[1+\sqrt{1+A_2}\right], \tag{3.4.4}$$

$$A_2 \equiv \frac{4}{\pi}\frac{V_f}{V_{Ea}}\frac{I}{W_b}\frac{p+1}{\phi_m}\,. \tag{3.4.5}$$

Eq.(3.4.4) is the new equation for the maximum amplitude ε_m of the E-field, which improves on Eq.(3.3.2) by accounting for polarization current effects. We find that we can neglect the polarization current effects on the value of ε_m if $A_2 \ll 1$ (i.e. for small beam density $\bar{n}_b$), in which case Eq.(3.4.2) reduces to previously derived (in Ref. [11]) Eq.(3.3.2). At the other extreme (for high beam density) when $\phi_m \ll 1$ the polarization current effects also can be neglected due to the weak logarithmic dependence (see Eq.(3.3.9, 3.3.10)) of the front velocity V_f on $\varepsilon(\phi_1)$ and $\bar{n}_b$. For the intermediate case (when neither $A_2 \ll 1$ nor $\phi_m \ll 1$ is satisfied) the numerical solution of Poisson's equation using Eq.(3.2.1, 3.2.2) has shown (see Figure 3.2) that the reduction of the ionization front velocity does not exceed 15 % ($p=0.3$, $n_0=3\cdot 10^{22}$/cc) and does not change the qualitative behavior described above.

3.5 Conclusions

We analyzed the propagation of a high energy density electron beam through a solid density insulator. The speed and structure of the ionization wave (supplying the return current electrons) created by the beam were found under the 1D steady propagation approximation. For small beam energy densities the front speed is limited by collisional ionization and decreases when going to higher beam densities (due to reduction in the beam Debye length). However, when the beam energy density $\bar{n}_b W_b$ exceeds a certain threshold, which is about 1% of the E-field energy density in the atom ($E_a^2/8\pi$), the ionization front speed increases due to the field ionization contribution. The contribution from field ionization starts to fall when the induced E-field becomes strong enough to neutralize itself (through field ionization followed by self-consistent charge neutralization). The resulting zigzag dependence of the ionization front velocity on the beam density (shown in Figure 3.2) allows for the development of instabilities (such as described in Ref.[11]). Such instabilities can have a negative impact on the quality of the proton beam by the electron beam.

We also found that the effect of the polarization current (caused by the E-field removing electrons from atoms) on the magnitude of the ionization front velocity is noticeable (up to 15% decrease at the velocity maximum, see Figure 3.2) but does not change the qualitative picture derived when neglecting it.

The results from the recent numerical modeling of beam propagation in insulators [10, 15] using Vlasov-Fokker-Planck and PIC codes are consistent with the developed model. In simulations the large amplitude E-field generated by the beam was observed and the importance of both the E-field ionization and collisional ionization was confirmed.

3.6 Acknowledgement

The text of Chapter 3, in part, includes material from “Impact of field ionization on the velocity of an ionization front induced by an electron beam propagating in a solid insulator” [B. Frolov, S. Krasheninnikov, A. Kemp, T. Cowan, New J. Phys **8**, 134 (2006)]. The dissertation author was the primary researcher.

3.7 Bibliography

[1] K. Krushelnik, E. L. Clark, M. Zepf, J. R. Davies, F. N. Beg, A. Machecek, M. I. K. Santala, M. Tatarakis, I. Watts, P. A. Norreys, and A. E. Dangor, *Phys. Plasmas* **7**, 2055 (2000)

[2] S. P. Hatchett, C. G. Brown, T. E. Cowan, E. A. Henry, J. S. Johnson, M. H. Key, J. A. Koch, A. B. Langdon, B. F. Lasinski, R. W. Lee, A. J. Mackinnon, D. M. Pennington, M. D. Perry, T. W. Phillips, M. Roth, T. C. Sangster, M. S. Singh, R. A. Snavely, M. A. Stoyer, S. C. Wilks, and K. Yasuike, *Phys. Plasmas* **7**, 2076 (2000)

[3] R. A. Snavely, M. H. Key, S. P. Hatchett, T. E. Cowan, M. Roth, T.W. Phillips, M. A. Stoyer, E. A. Henry, T. C. Sangster, M. S. Singh, S. C. Wilks, A. MacKinnon, A. Offenberger, D.M. Pennington, K. Yasuike, A. B. Langdon, B. F. Lasinski, J. Johnson, M. D. Perry, and E. M. Campbell, *Phys. Rev. Lett.* **85**, 2945 (2000)

[4] A. J. Mackinnon, M. Borghesi, S. Hatchett, M. H. Key, P. K. Patel, H. Campbell, A. Schiavi, R. Snavely, S. C. Wilks, and O. Willi, *Phys. Rev. Lett.* **86**, 1769 (2001)

[5] M. Tabak, J. Hammer, M. E. Glisky, W. L. Kruer, W. C. Wilks, and R. J. Mason, *Phys. Plasmas* **1**, 1626 (1994); J. Lindl, *Phys. Plasmas* **2**, 3933 (1995)

[6] R. R. Wilson, *Radiology* **47**, 487 (1946)

[7] V. Tikhonchuk, *Phys. Plasmas* **9**, 1416 (2002)

[8] J. Fuchs, T. E. Cowan, P. Audebert, H. Ruhl, L. Gremillet, A. Kemp, M. Allen, A. Blazevic, J.-C. Gauthier, M. Geissel, M. Hegelich, S. Karsch, P. Parks, M. Roth, Y. Sentoku, R. Stephens, and E. M. Campbell, *Phys. Rev. Lett*. **91**, 255002 (2003)

[9] L. Gremillet, F. Amiranoff, S. D. Baton, J.-C. Gauthier, M. Koenig, E. Martinolli, F. Pisani, G. Bonnaud, C. Lebourg, C. Rousseaux, C. Toupin, A. Antonicci, D. Batani, A. Bernardinello, T. Hall, D. Scott, P. Norreys, H. Bandulet, and H. Pépin, *Phys. Rev. Lett.* **83**, 5015 (1999)

[10] A. Kemp, Robert E. W. Pfund, and Jürgen Meyer-ter-Vehn*, Phys. Plasmas* **11**, 5648 (2004)

[11] S. Krasheninnikov, A. V. Kim, B. K. Frolov, R. Stephens*, Phys. Plasmas* **12**, 073105 (2005)

[12] R. Stephens R. A. Snavely, Y. Aglitskiy, F. Amiranoff, C. Andersen, D. Batani, S. D. Baton, T. Cowan, R. R. Freeman, T. Hall, S. P. Hatchett, J. M. Hill, M. H. Key, J. A. King, J. A. Koch, M. Koenig, A. J. MacKinnon, K. L. Lancaster, E. Martinolli, P. Norreys, E. Perelli-Cippo, M. Rabec Le Gloahec, C. Rousseaux, J. J. Santos, and F. Scianitti*, Phys. Rev. E* **69**, 066414 (2004)

[13] M. Honda, J. Meyer-ter-Vehn, A. Pukhov, *Phys. Rev. Lett.* **85**, 2128 (2000)

[14] A. Kemp*, Fourth International Conference on Inertial Fusion Science and Applications (IFSA 2005), Biarritz, France* (2005)

[15] A. P. L. Robinson, A. R. Bell, and R. J. Kingham, *Plasma Phys. Control. Fusion* **48**, 1063 (2006)

4

Beam Propagation Through a Gas

4.1 Introduction

The generation of hot electron beams by intense lasers and propagation of these beams in matter [1] were studied extensively in a number of recent works [2-13]. In particular, the beam propagation in insulators was studied to find the impact of the ionization processes on the beam [6-10, 12, 13]. The propagation velocity of an intense electron beam in an insulator is determined by the velocity of the beam-induced ionization wave which creates enough electrons and ions to neutralize beam charge and current. If the beam density is larger than the electron density that could be provided by ionization, only a fraction of the beam density would be allowed to propagate (to have return current velocity smaller than beam velocity [1]).

In the experiment described in the paper by Batani et al. [6] the atomic gas density was $\leq 3 \cdot 10^{19}\,\mathrm{cm}^{-3}$ while the initial electron beam (generated by a high-intensity laser pulse in a thin metallic (Ti) target) was estimated to have density $\sim 5 \cdot 10^{20}\,\mathrm{cm}^{-3}$ and energy ~1 MeV. The ionization cloud expansion velocity observed in the experiment was about c/30 to c/10, where c is the speed of light. The large amplitude electrostatic field created by fast electrons was suggested to be responsible for ionization at such low gas densities. Indeed, in the absence of field ionization the speed of the ionization front v_f can be estimated as $v_f \sim \nu_{ea}\lambda_{Db} \propto n_0/\sqrt{n_b}$, where ν_{ea} is the rate of ionization (per beam electron) due to electron-atom collisions; λ_{Db} is the beam Debye length; n_0 and n_b are the gas and beam densities. In this simple estimate the Debye length shows how far the beam can penetrate and ν_{ea} shows how fast the gas is ionized inside the beam. For relativistic beam energies, $W_b \gtrsim 0.5\,\mathrm{MeV}$, the resulting collisional ionization front velocity would be less then $c/10^4$ for gas densities $\lesssim 10^{20}\,\mathrm{cm}^{-3}$ (assuming that beam density equals gas density). Notice that if $n_b \ll n_0$ (as in [8] where solid density insulators were considered) the collisional ionization front is much faster for a given beam density due to faster ionization.

In Ref. 6 the return current velocity was used as the estimate of the ionization front velocity. The amplitude of the induced E-field was assumed to be large enough to neglect the time required for field ionization. The secondary electrons were assumed to be ‘cold’ and, therefore, strongly collisional. The front velocity was estimated to be $c_f \approx \sqrt{eE\lambda_{ii}/mc^2}$ (see Eq.(3) in Ref. 6), where the interionic distance, λ_{ii}, is used as a mean free path for beam electrons. This estimate produced the return current velocity amplitude of about c/20 for the conditions described above. However, considering that the strong E-field quickly accelerates the return current electrons to energies comparable to the beam potential (~1MeV) due to a “runaway” effect at low densities (see, for example, Ref. 7) the secondary electrons cannot be considered as ‘cold’. Therefore, the use of the interionic distance λ_{ii} (which is about 10^{-6} cm for gas density 10^{19} cm^{-3}) as a mean free path (which is about 10^{-3} cm for electron energies above 10 eV) seems to underestimate the mean free path and, therefore, the return current velocity by orders of magnitude. The reference given in the text does not seem to support this approximation either. Instead, the beam propagation velocity is rather limited by the rate of the field ionization happening in a narrow layer within the Debye length λ_D. The corresponding velocity estimate is $v_f \sim \nu_{EI}(E)\lambda_D \propto \exp(-E_a / E)$, where E_a is the atomic E-field, and $\nu_{EI}(E)$ is the field ionization frequency (see, for example Ref. 14). For the E-field amplitude $E \sim 0.1E_a$ (see Ref. 7), the front velocity would be about c/20 if the ionization layer width is about λ_D/20. This is consistent with the results of Ref. 7. To obtain a more solid estimate the self-consistent treatment of field ionization, electron acceleration and space charge balance is required.

In Ref. 7 the simple model of the ionization front induced by the beam electrostatic field was analyzed. In the model the ions were assumed immobile and the beam electron density profile was fixed and determined by their energy distribution. The secondary electrons were generated in the strong E-field region by field ionization and subsequently accelerated, producing the return current. The collisionless approximation was used for secondary electrons due to low gas density (weak friction force can not balance acceleration in the strong field). For the case of large atom densities one would have to use the drift approximation as described in [8]. The velocity of the front was found for sub-relativistic values of the beam energy. In this work we generalize and verify the approach developed in Ref. 7 to include relativistic beam energies and find the approximate analytical expression for the ionization front velocity and corresponding beam density which is allowed to propagate in a gas.

In the next section we find the electron density from the collisionless kinetic equation, substitute it into Poisson's equation and show the corresponding numerical solutions. In Section 4.3 we derive the approximate analytical solution of that equation. We show that the experimental results from Ref. 6 can be closely recovered using our model, assuming the maximum energy in the beam to be $W_b \sim 0.5\ \mathrm{MeV}$. The conclusions are drawn in Section 4.4.

4.2 Relativistic equation derivation

The low density of the gas allows us to neglect collisional ionization and assume that secondary electrons are collisionless. We start with the steady state 1V1D relativistic electron kinetic equation in the ionization front frame

$$\frac{\partial f}{\partial x} v(p) + e\frac{\partial \varphi}{\partial x}\frac{\partial f}{\partial p} = S(x,p)\,,\ \ S(x,p) = \left(n_0 - n_i(x)\right)\nu_{EI}(x)\cdot\delta\left(p - p_f\right), \qquad (4.2.1)$$

where e is the elementary charge and p is the electron momentum; φ is the electrostatic potential; S(x,p) is the ionization source, where we assume that the newborn electrons are at rest in the laboratory (gas) frame and, therefore, have momentum $p_f \equiv p(v = -v_f)$ in the moving frame; $\nu_{EI}(x)$ is the field ionization rate; n_0 and n_i are gas and ion densities. The total energy of electron is $\xi(x,p) = (p^2 + m^2c^2)^{1/2}c - e\varphi(x)$ and by changing the variables set from (x, p) to (x, ξ) we eliminate the field term in Eq.(4.2.1) and find $f(x,\xi) = -\int_x^{x_0} S(x',\xi)/v(x',\xi)dx'$, where x_0 corresponds to the position of the beam head.

To find the electron density we need to integrate $f(x,\xi)$ over the momentum space. Using the energy conservation $\xi(x,p)=\xi(x',p')$ we can express the electron momentum p as $p=p\bigl(x,\xi(x',p')\bigr)$. That allows us to change the integration variable from p to p' to use the δ-function in S

$$n_e(x)=-\int_x^{x_0}\int_0^{\infty}\bigl(S(x',\xi)/v(x',\xi)\bigr)(\partial p/\partial p')dp'dx'. \qquad (4.2.2)$$

From $\partial\xi/\partial p=v(x,\xi)$ we have $\partial p/\partial p'=v(x',\xi)/v(x,\xi)$. Using $v=-c/\sqrt{1+(mc/p)^2}$ we find

$$v(x,\xi)\big|_{p'=p_f}=-c\sqrt{1-\left\{\bigl(1-(v_f/c)^2\bigr)^{-1/2}+e\bigl(\varphi(x')-\varphi(x)\bigr)/mc^2\right\}^{-2}}, \qquad (4.2.3)$$

We can use Eq.(4.2.2-3) to find ion density (Z=1) by replacing m with the ion mass m_i. The potential term in Eq.(4.2.3) becomes (m_i/m) times smaller and can be neglected. Therefore, for ions we have $v(x,\xi)\big|_{p'=p_f}=-v_f$, and Eq.(4.2.3-4) yield the integral equation which has the solution

$$n_i(x)=n_0\bigl(1-G(x)\bigr),\ G(x)=\exp\left\{-\int_x^{x_0}\nu_{EI}(x')dx'/v_f\right\}. \qquad (4.2.4)$$

Now we can use Eq.(4.2.2-4) to write the final expression for the electron density

$$n_e(x)=-n_0\int_x^{x_0}\bigl(v_f/v(x,x')\bigr)(dG/dx)dx'. \qquad (4.2.5)$$

The stationary density of beam electrons is a function of the potential. The form of the function is determined by the beam energy distribution function. We follow Ref. 7 and use the beam density profile $n_b(\varphi)=\bar{n}_b[e\varphi/W_b]^p$, where W_b is the maximum beam energy in the front frame; $\bar{n}_b$ is the maximum beam density. This profile ensures that the beam has zero density at its head. Since the beam density is an explicit function of the potential φ it is convenient to use the potential φ as the main variable instead of the space coordinate x. Then the Poisson's equation has the form

$$d(E^2/2)/d\varphi = -4\pi e\left\{n_i(\varphi) - n_e(\varphi) - \bar{n}_b\{e\varphi/W_b\}^p\right\}. \qquad (4.2.6)$$

Using the expression for densities found in Section II and introducing the dimensionless variables $\psi = e\varphi/W_b$ and $\varepsilon = -E/E_a$ and the dimensionless parameters $c_f = v_f/c$, $W_c = W_b/mc^2$, and $\eta_b = \bar{n}_b/n_0$ we can rewrite Eq.(4.2.6) as

$$d(\varepsilon^2/2)/d\psi = P_0\left\{\eta_b\psi^p + \int_0^{\psi}\left(1 - 1/V_c(\psi,\psi')\right)(\partial G/\partial\psi')d\psi'\right\}, \qquad (4.2.7)$$

$$V_c(\psi,\psi') \equiv |v|/v_f = \sqrt{1-(1-c_f^2)/(1+(\psi-\psi')\cdot\alpha)^2}\,/c_f\,, \qquad (4.2.8)$$

where $\alpha = W_c\sqrt{1-c_f^2}$; $P_0 \equiv 4\pi W_b n_0/E_a^2$; $E_a = (2/3)(I_a/I_H)^{5/2} e/a_b^2$; $I_H = e^4 m/(2\hbar^2)$; $a_b = \hbar^2/e^2 m$ and I_a is the gas ionization potential. The effective frequency of the field ionization [14] is $\nu_{EI}(\varepsilon) = \nu_0\exp(-1/\varepsilon)/\varepsilon$, $\nu_0 = 6me^4/\hbar^3$, and

$$G(\psi) = \exp\left\{-(\xi_{bc}/c_f)\int_0^{\psi}(\nu(\varepsilon)/\varepsilon)d\psi'\right\}, \quad \xi_{bc} = 4.5W_c\sqrt{mc^2/I_H}\,(I_H/I_a)^{5/2}, \qquad (4.2.9)$$

where we introduced $\nu(\varepsilon) \equiv \exp(-1/\varepsilon)/\varepsilon$. The absence of the E-field outside of the ionization wave provides us with two boundary conditions (BCs) for Eq.(4.2.7), and to ensure that there is no space charge behind the front, we impose an additional BC

$$\varepsilon(\psi=0) = \varepsilon(\psi=1) = 0\,,\ d(\varepsilon^2/2)/d\psi\Big|_{\psi=1} = 0 \qquad (4.2.10)$$

These three BCs for the first order differential equation can all be satisfied only by adjusting two free parameters in the equation. We choose these two parameters to be c_f and η_b. We solve Eq.(4.2.7-10) numerically for a set of gas densities n_0, beam energies W_b, and values of smoothness parameter p. By choosing the appropriate ionization potential, we simulate two different gases, argon and helium. The calculated value of the front velocity c_f is plotted in Figures 4.1-4 as a function of gas density.

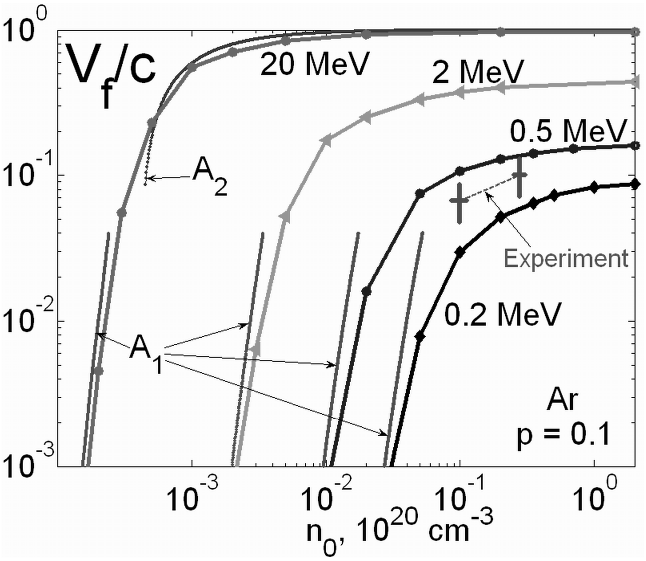

Figure 4.1. The values of the ionization front velocity obtained by numerical solution of Eq.(4.2.7-10) are plotted for argon with p = 0.1. The asymptotic analytical solutions are plotted for two limits when c_f <<1 and 1-c_f<<1, curves ‘A_1’ and A_2’ respectively. The experimental results for argon from Ref. 6 are shown by the “Experiment” data points.

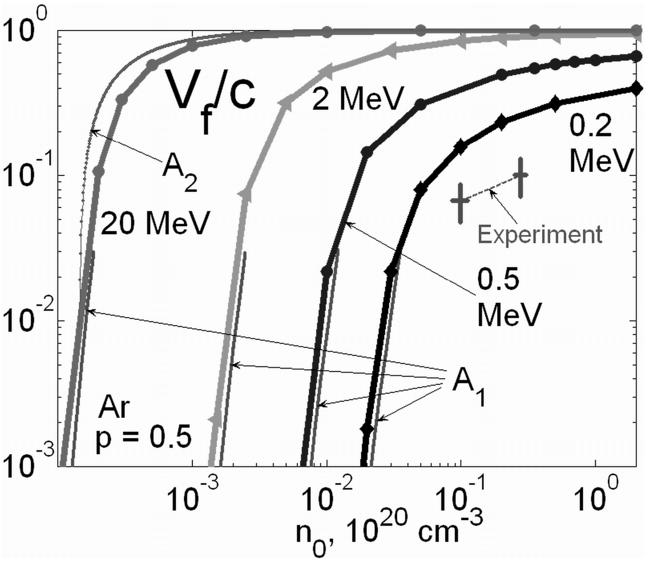

Figure 4.2. Same as Figure 4.1 but with p = 0.5 for argon.

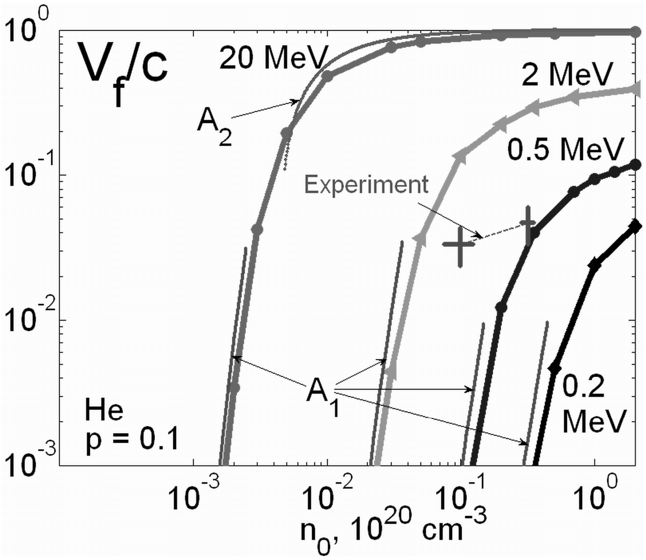

Figure 4.3. Same as Figure 4.1 but for helium with p = 0.1.

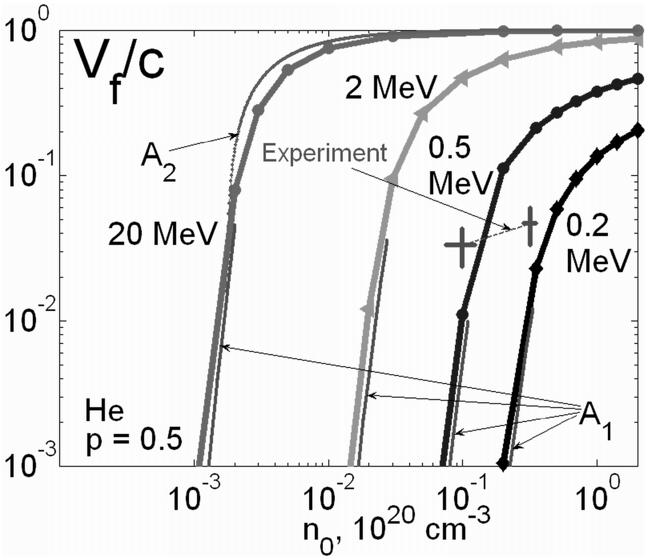

Figure 4.4. Same as Figure 4.1 but for helium with p = 0.5.

To verify the model, first, we successfully recovered the simulation results from the previously analyzed non-relativistic case [7]. Second, the ionization front velocity values for the experiments with argon and helium in Ref. 6 were calculated. The experimentally measured velocity values in Ref. 6 are closely recovered by our model for both argon and helium, assuming that the beam energy was ~0.5 MeV and p ~ 0.1 (see Figure 4.1, 4.3). The front velocity values for p = 0.5 are shown for comparison in Figures 4.2, 4.4. The beam energy distribution underlying the beam density profile $n_b(\psi) = \bar{n}_b \psi^p$ and its dependence on p are discussed in Ref. 7, 15. The propagating beam density predicted by our model is about 90-99% of the gas density, and the agreement with experiment seems to be better for argon. In the next sections, we analyze Eq.(4.2.1-4) and find the approximate expression for the front velocity in the limits of small and large velocities.

Note that the beam density n_b and beam energy W_b are given in the front frame moving with the velocity v_f. The maximum beam energy in the gas frame W_{lab} can be calculated from W_c using Lorentz velocity transformation

$$W_{lab} = mc^2 \left\{ (1 + c_b c_f) / \left((1 - c_b^2)(1 - c_f^2) \right)^{1/2} - 1 \right\}, \; c_b^2 \equiv 1 - (1 + W_c)^{-2}. \qquad (4.2.11)$$

4.3 Front velocity estimate

Considering the exponential dependence of the field ionization rate on the E-field amplitude, the reasonable assumption to make is that all ionization happens in a narrow region near the maximum value $\varepsilon_I = \varepsilon(\psi_I)$ of the E-field, where the E-field amplitude can be approximated with parabola (since $d\varepsilon / d\psi = 0$ at ψ_I)

$$\varepsilon(\psi \approx \psi_I) \approx \varepsilon_I + \varepsilon_I^{//} (\psi - \psi_I)^2 / 2, \; \varepsilon_I^2 = 2 P_0 \eta_b \psi_I^{p+1} / (1 + p) \qquad (4.3.1)$$

where the maximum value of the E-field in the front, ε_I, is estimated from the Poisson's equation where we neglect the induced space charge term (whose integral contribution is small for $\psi < \psi_I$). By substituting Eq.(4.3.1) into definition of G in Eq.(4.2.9) we find

$$G(\psi_I) \approx \exp\left\{-\sqrt{-0.5\pi\varepsilon_I^2 / \varepsilon_I^{//}} / \Delta\psi_I\right\}, \quad \Delta\psi_I \equiv \left| d\ln G / d\psi \right|_{\psi_I}^{-1} = c_f \varepsilon_I / \left(\xi_{bc} \nu(\varepsilon_I)\right). \quad (4.3.2)$$

Note: due to the assumed symmetry of the E-field around ψ_I (see Eq.(4.4.1)) the integral in Eq.(4.3.4) will double if we integrate over the whole ionization region instead of just half of it, i.e. $G(\psi = 1) \approx G^2(\psi_I)$. From Eq.(4.3.2), we find the expression for $\varepsilon_I^{//}$, which can be combined with the expression for $\varepsilon_I^{//}$ found by differentiating Eq.(4.2.7)

$$\varepsilon_I^{//} = (p\eta_b \psi_I^{p-1} + I_2) P_0 / \varepsilon_I, \quad I_2 \equiv \int_0^{\psi_I} \left\{\partial\left(1 - 1/V_c(\psi_I, \psi')\right) / \partial\psi'\right\} (\partial G / \partial\psi') d\psi'. \quad (4.3.3)$$

If the maximum potential energy gain W_c is much larger than the electron initial kinetic energy plus its rest mass, i.e. $\alpha >> 1$, we have from Eq.(4.2.8)

$$1 / V_c(\psi, \psi') \approx c_f, \quad I_2 \approx -(1 - c_f) G_I / \Delta\psi_I. \quad (4.3.4)$$

Combining the two expressions for $\varepsilon_I^{//}$, we find the thickness of the ionization region $\Delta\psi_I$ and then use Eq.(4.3.2) to find c_f

$$\Delta\psi_I \approx \varepsilon_I \psi_I \pi (1 - G_I) / \left((1 + p) G_I \ln^2 G_I\right), \quad (4.3.5)$$

$$c_f \approx \psi_I \xi_{bc} \nu(\varepsilon_I) \pi (1 - G_I) / \left((1 + p) G_I \ln^2 G_I\right). \quad (4.3.6)$$

To find c_f we need to estimate the values of ψ_I, G_I and ε_I. First, we apply Eq.(4.2.7) at $\psi = 1$ and ψ_I

$$\eta_b \approx (1 - c_f)(1 - G(1)), \quad \eta_b \psi_I^p \approx (1 - c_f)(1 - G_I). \quad (4.3.7)$$

Then the third equation comes from the integration of Eq.(4.2.7) over ψ from 0 to 1 (see Appendix B)

$$\eta_b/(1+p) \approx (1-c_f)(1-G(1))(1-\psi_I)\,. \tag{4.3.8}$$

The combination of Eq.(4.3.7-8) allows us to find $\psi_I = p/(1+p)$. Using $G(\psi=1) \approx G^2(\psi_I)$ and Eq.(4.3.7), we obtain

$$G_I = \psi_I^{-p} - 1\,,\ \eta_b = (1-c_f)(1-G_I)\psi_I^{-p}\,. \tag{4.3.9}$$

In the case of full (or almost full) ionization, G(1)<<1, the better agreement is achieved using the approximation $G(1) \approx 0$, which produces

$$G_I = 1-\psi_I^{p}\,,\ \eta_b = 1-c_f\,. \tag{4.3.10}$$

The values of ψ_I and G_I from Eq.(4.3.10) are shown in Figure 4.5 against the profiles of ε and G obtained from numerical solution of Eq.(4.2.7-10). The estimate of η_b from Eq.(4.3.10) is plotted in Figure 4.6 against the values of η_b obtained in simulation. We also plotted the values of α in Figure 4.7 to verify the assumption $\alpha >> 1$.

Substituting Eqs.(4.3.1, 4.3.9) into Eq.(4.3.6) we find the equation for ε_I

$$1 = \frac{\varepsilon_I^2}{P_0}\frac{1+p}{2\psi_I}\frac{1}{1-G_I} + \frac{\pi\psi_I}{1+p}\frac{1-G_I}{G_I \ln^2 G_I}\xi_{bc}\nu(\varepsilon_I)\,. \tag{4.3.11}$$

This equation does not have a simple solution and we consider instead two possible limits for system consisting of Eqs.(4.3.1, 6, 9). In the slow front limit c_f <<1, we can find ε_I from Eqs.(4.3.1, 4.3.9) neglecting c_f compared to 1. The corresponding solution is shown as curve A_1 in Figures 4.1-4. In the limit c_f ~ 1, we can find ε_I from Eq.(4.3.6) (assuming $c_f \approx 1$), and then we find c_f from Eq.(4.3.1, 4.3.9) (this asymptotic solution is shown as curve A_2 in Figures 4.1-4.)

$$c_f = 1 - (1+p)\varepsilon_I^2 / \left((1-G_I)2\psi_I P_0\right). \tag{4.3.12}$$

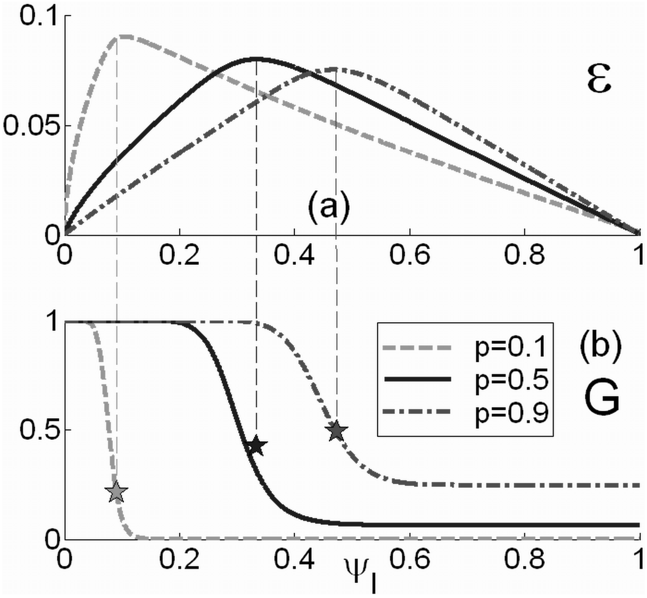

Figure 4.5. The profiles of the normalized E-field ε (a) and atom density G (b) are plotted as functions of the normalized potential ψ. Different lines correspond to different values of the beam density smoothness parameter p, p = {0.1,0.5,0.9}. The values of other parameters are the same (W_b = 20 MeV, $n_0 = 10^{17}\,\mathrm{cm}^{-3}$, I_a= 15.76 eV [Ar]) except for c_f = {0.52,0.78,0.75} and η_b= {0.48,0.21,0.19}, respectively. Stars show the analytical estimate of the position of the E-field maximum and corresponding value of density of atoms G_I (see Eq.(4.3.10)).

If $\alpha \ll 1$ the electron velocity can be written as $\sqrt{c_f^2 + 2(1-c_f^2)(\psi - \psi')\alpha}$. It can be shown that if the acceleration potential W_c is too small compared to c_f^2, $\alpha \ll c_f^2/2$, no solution exists. For the intermediate case, $c_f^2/2 \ll \alpha \ll 1$, we recover Eq.(4.3.6), which is equivalent to the result obtained in [7]. The approximate solutions given in Eq.(4.3.6) and Eq.(4.3.12) are shown in Figures 4.1-4 (curves A_1 and A_2 respectively) together with the corresponding numerical solution.

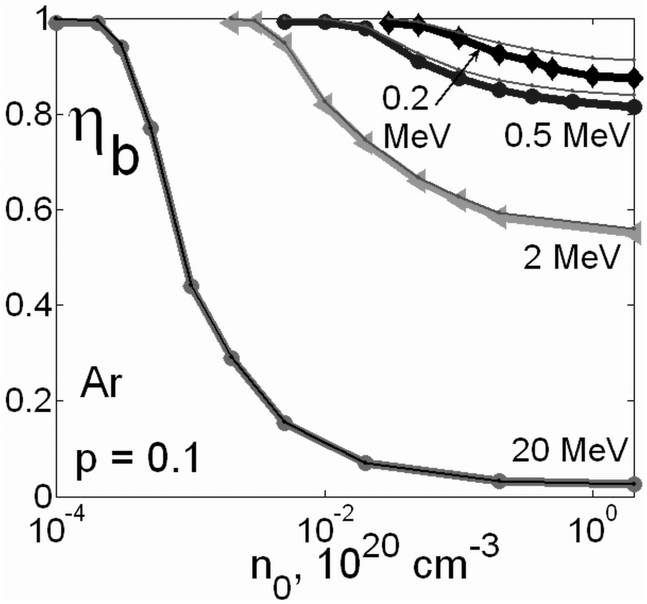

Figure 4.6. The ratio of the beam density to the gas density (for argon with p = 0.1) is given as a function of gas density for the set of beam energies (0.2, 0.5, 2 and 20 MeV; thick curves). Thin curves correspond to the estimation given in Eq.(4.3.10).

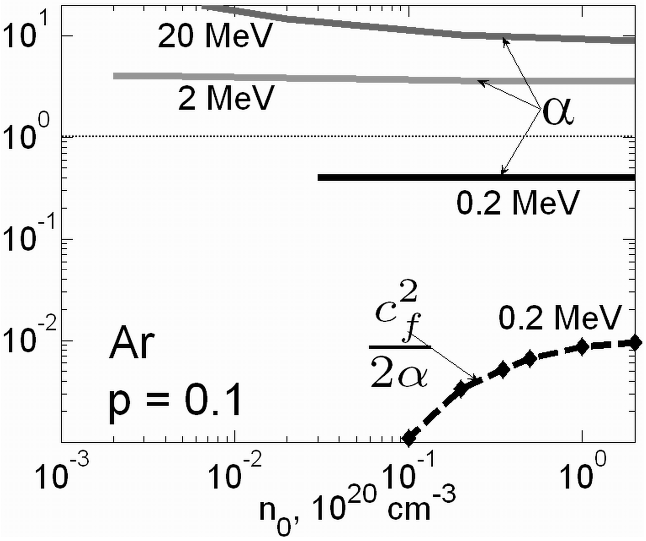

Figure 4.7. The values of the parameter $\alpha \equiv W_c\sqrt{1-c_f^2}$ are shown (to verify that $\alpha >> 1$) for a set of numerical solutions shown in Figure 4.1. The data are given for argon with p = 0.1 and W_b = 2 and 20 MeV. For W_b = 0.2 MeV the values of parameters α and $c_f^2/2\alpha$ are also plotted to verify that $c_f^2/2 << \alpha << 1$.

When deriving one of the key equations, Eq.(4.3.8) (see Appendix B), we assumed that the derivative $dG/d\psi$ peaks close to ψ_I and also that $1-\psi_I << \Delta\psi_I$. To verify these assumptions we use the resulting expression for $\Delta\psi_I$ from Eq.(4.3.5) to rewrite these conditions in the form

$$1 << S(p) \equiv (1-G_I)/(G_I \ln^2 G_I) << (1-\psi_I)(1+p)/(\psi_I \pi \varepsilon_I) . \qquad (4.3.13)$$

It can be shown that S(p)>1.5 for any p, and the condition S(p)>>1 is almost always satisfied. The second condition, $1-\psi_I >> \Delta\psi_I$, is satisfied if p is not too large (see Figure 4.8).

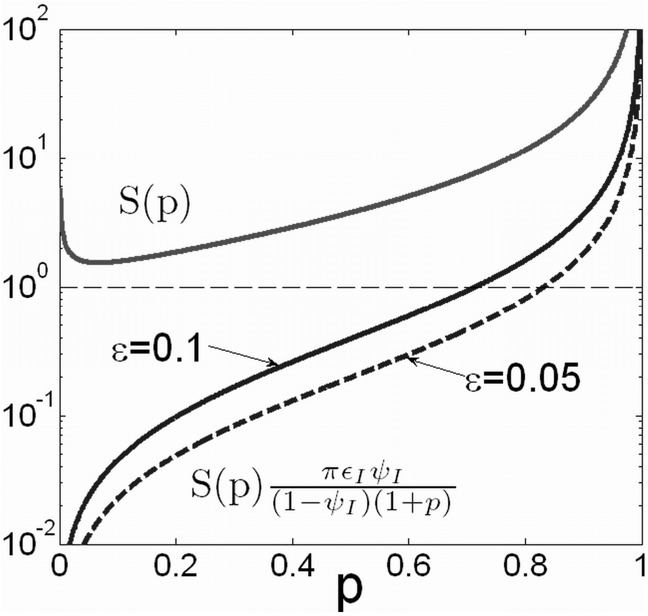

Figure 4.8. The value of the parameter S(p) defined in Eq.(4.2.13) is given as a function of the beam density smoothness p to verify the assumption $\psi_I \approx \psi_G$, which requires S(p)>>1. The other assumption, $1-\psi_I >> \Delta\psi_I$, requires that $S(p)\pi\varepsilon_I\psi_I/[(1+p)(1-\psi_I)] << 1$, and the corresponding curve is shown for two values of ε_I. The latter condition is satisfied only if p is not too large.

In this treatment, we neglected collisional ionization, but it becomes important at small densities when the induced E-field becomes too small compared to the atomic field E_a. Using the estimate of the velocity of a pure collisional front $c_f \sim \nu_{ea}\lambda_{Db}/c$, and using Eq.(4.3.6), we estimate that collisional ionization is important if $n_b \lesssim W_c^{-1} \cdot 4 \cdot 10^{17}\,\mathrm{cm}^{-3}$ (see also [7]). At large beam densities and relativistic velocities the collisional ionization becomes important when $\nu_{ea}\lambda_{Db}/c \sim 1$, which requires $n_b \gtrsim W_c \cdot 10^{28}\,\mathrm{cm}^{-3}$ (that, however, is much larger than the density of laser generated beams ~$10^{21}\mathrm{cm}^{-3}$).

4.4 Conclusions

The ionization front induced by a high-energy and high-density electron beam in gas was studied in 1-D approximation. We generalized the approach developed in [7] to include the relativistic beam energies. The approximate expression for the beam density and the new expression for the corresponding front velocity in the limit of large and small front velocities (see Figures 4.2, 4.4) were derived. The values of beam density and front velocity were calculated for a wide range of beam energies and gas densities through the numerical solution of new relativistic Eqs.(4.2.1-2) and verified against the analytical estimates. The calculated front velocity is in good agreement with the experimental data for helium and argon from [6]. However, in [6] the return current velocity was assumed to limit the ionization front velocity. Instead, as we have shown, the beam propagation velocity is rather limited by the rate of the field ionization happening in a narrow layer within the Debye length λ_D.

4.5 Acknowledgement

The text of Chapter 4, in part, includes material from “The propagation of a dense relativistic electron beam through a gas” [B.K. Frolov, and S.I. Krasheninnikov, to appear in October 2006 in Phys. Plasmas]. The dissertation author was the primary researcher.

4.6 Bibliography

[1] R. B. Miller, *An introduction to the physics of intense charged particle beams*, New York: Plenum (1982)

[2] M. Tatarakis, J. R. Davies, P. Lee, P. A. Norreys, N. G. Kassapakis, F. N. Beg, A. R. Bell, M. G. Haines, and A. E. Dangor, *Phys. Rev. Lett*. **81**, 999 (1998)

[3] K. B. Wharton, S. P. Hatchett, S. C. Wilks, M. H. Key, J. D. Moody, V. Yanovsky, A. A. Offenberger, B. A. Hammel, M. D. Perry, and C. Joshi, *Phys. Rev. Lett*. **81**, 822 (1998)

[4] T. A. Hall, S. Ellwi, D. Batani, A. Bernardinello, V. Masella, M. Koenig, A. Benuzzi, J. Krishnan, F. Pisani, A. Djaoui, P. Norreys, D. Neely, S. Rose, M. H. Key, and P. Fews, *Phys. Rev. Lett*. **81**, 1003 (1998)

[5] R. A. Snavely, M. H. Key, S. P. Hatchett, *Phys. Rev. Lett* **85**, 2945 (2000)

[6] D. Batani, S. D. Baton, M. Manclossi, J. J. Santos, F. Amiranoff, M. Koenig, E. Martinolli, A. Antonicci, C. Rousseaux, M. Rabec Le Gloahec, T. Hall, V. Malka, T. E. Cowan, J. King, R. R. Freeman, M. Key, and R. Stephens, *Phys. Rev. Lett.* **94**, 055004 (2005)

[7] S. I. Krasheninnikov and B. K. Frolov, *Phys. Plasmas* **13**, 033101 (2006)

[8] S. I. Krasheninnikov, A. V. Kim, B. K. Frolov, and R. Stephens, *Phys. Plasmas* **12**, 073105 (2005)

[9] V. T. Tikhonchuk, *Phys. Plasmas* **9**, 1416 (2002)

[10] A. J. Kemp, Robert E. W. Pfund, and Jürgen Meyer-ter-Vehn, *Phys. Plasmas* **11**, 5648 (2004); A. J. Kemp, Y. Sentoku, T. Cowan, J. Fuchs, and H. Ruhl, *Phys. Plasmas* **11**, L69 (2004)

[11] M. Tatarakis, J. R. Davies, P. Lee, P.A. Norreys, N. G. Kassapakis, F. N. Beg, A. R. Bell, M. G. Haines, and A. E. Dangor, *Phys. Rev. Lett.* **81**, 999 (1998); M. Tatarakis, F. N. Beg, E. L. Clark, A. E. Dangor, R. D. Edwards, R.G. Evans, T. J. Goldsack, K.W. D. Ledingham, P. A. Norreys, M. A. Sinclair, M-S.Wei, M. Zepf, and K. Krushelnick, *Phys. Rev. Lett.* **90**, 175001 (2003)

[12] M. Manclossi, J. J. Santos, D. Batani, J. Faure, A. Debayle, V. T. Tikhonchuk, and V. Malka, *Phys. Rev. Lett.* **96**, 125002 (2006)

[13] D. Batani, Proceedings of Invited Papers, *33rd European Physical Society Conference on Plasma Physics,* Roma, Italy, 2006 (http://eps2006.frascati.enea.it/invited/index.htm)

[14] M. V. Ammosov, N. B. Delone, and V. P. Krainov, *Sov. Phys. JETP* **64**, 1191 (1986)

[15] B. Frolov, S. Krasheninnikov, A. Kemp, T. Cowan, *New J. Phys* **8**, 134 (2006)

5

Conclusions

In this dissertation a systematic study of fast electron transport in the Inertial Fusion problems was presented. The principal result of this work can be classified into three major categories: *heat conduction in the semi-collisionless regime, propagation of ionization wave induced by the intense electron beam in solid insulators* and *propagation of the ionization wave induced by the intense electron beam in gases.*

In the first category we studied the electron heat transport and found two possible approaches allowing to improve the accuracy of the heat conduction description in the semi-collisionless regime. In the first approach three scalar moments (as opposed to two in the fluid and Grad's models) were used to describe the electron energy distribution function. As a result the heat flux can be accurately calculated for the values of the Knudsen number (the ratio of the mean free path to the characteristic temperature space scale) approaching 0.1 (as oppose to just 0.01 for fluid model). In the second approach (where we also account for the B-field) the approximate solution of the kinetic equation is found assuming that at low energies the electron distribution function is close to Maxwellian. The resulting distribution is determined nonlocally by the surrounding temperature profile. The corresponding expression for the heat flux is quite accurate for values of the Knudsen number up to 1 and can be used in the presence of the B-field. Both methods allow the description of the distribution function in greater details and provide results consistent with the kinetic model and each other. The difference in the form of the final expression for the heat conduction allows one to choose the approach which fits particularly well the given hydro code and the simulated problem.

In the second category the electron beam propagation in a solid insulator was studied. We analyzed the behavior of the induced ionization wave and found the wave velocity as a function of the beam density. For small beam energy densities the front speed is limited by collisional ionization and decreases when going to higher beam densities (due to reduction in the beam Debye length). However, when the beam energy density exceeds a certain threshold, which is about 1% of the E-field energy density in the atom ($E_a^2/8\pi$, where $E_a = 5.1 \cdot 10^9\,\mathrm{V/cm}$ for hydrogen), the ionization front speed jumps up due to the field ionization contribution. The further increase in the beam density results in a slow decline of the velocity. The slowing of the wave is caused by the rapid field-ionization at high beam densities resulting in the self-screening of the induced E-field. The resulting S-shaped dependence of the ionization wave velocity on beam density can be responsible for filamentation-type instabilities seen in experiments. The developed model of beam propagation in insulators is confirmed by the results from numerical modeling using Vlasov-Fokker-Planck and PIC codes.

In the third category we analyzed the relativistic beam propagation through a gas. We found that for low gas densities the ionization front velocity is much less than the speed of beam electrons. The reason is that the front velocity strongly depends on the gas density due to the exponential dependence of the field ionization rate on the induced E-field in the absence of collisional ionization. This result explains the slow ionization wave propagation in gases at atmospheric pressure observed in experiments.

A

Units and Conventions

All units are CGS except where noted.

B

Total Charge

If we integrate Eq.(4.2.7) from 0 to 1 and use first two BCs given in Eq.(4.2.10) we obtain

$$\eta_b/(1+p) = -\int_0^1 H(\psi')(\partial G/\partial\psi')d\psi', \tag{B.1}$$

$$H(\psi') \equiv 1-\psi' - (c_f/\alpha)\left\{\sqrt{[1+(1-\psi')\alpha]^2-(1-c_f^2)}-c_f\right\}, \tag{B.2}$$

where we changed the order of integration. We cannot directly calculate the second integral over ψ' in Eq.(B.1) because we don't know the E-field (required by the function G) but we can try to estimate it. The function $dG/d\psi'$ is relatively large only in a narrow region near $\psi_G : d^2G/d\psi^2 = 0$, while the function $H(\psi')$ is quite smooth. The equation for ψ_G, $d^2G(\psi_G)/d\psi^2 = 0$, can be rewritten in the form similar to Poisson's equation

$$\varepsilon'(\psi_G) = [\xi_b \nu\varepsilon/(1-2\varepsilon)]_{\psi_G}. \tag{B.3}$$

The equation for ψ_I is simply $\varepsilon'|_{\psi_I} = 0$, and we can use approximation $\psi_G \approx \psi_I$ if the right hand side of Eq.(B.3) is much smaller than any of two terms in the Poisson's equation. That condition after some algebra reduces to

$$\Delta\psi_I >> 2\psi_I \varepsilon_I / [(1 - 2\varepsilon_I)(1 + p)]. \tag{B.4}$$

Therefore, if G profile is not too steep the smooth function under the integral over ψ' can be approximated by its value taken at $\psi_I \approx \psi_G$

$$\int_0^1 H(\psi')(\partial G / \partial\psi') d\psi \approx -[1 - G(1)] H(\psi_I) . \tag{B.5}$$

For $\alpha >> 1$ we can estimate (assuming $|H(\psi_I) / H'(\psi_I)| = 1 - \psi_I >> \Delta\psi_I$)

$$\eta_b / (1 + p) \approx [1 - G(1)](1 - c_f)(1 - \psi_I) . \tag{B.6}$$

For $c_f^2 / 2 << \alpha << 1$ this approach yields

$$\eta_b / (1 + p) \approx [1 - G(1)] \cdot [c_f^2 / 2\alpha] \cdot \left[\sqrt{1 + 2\alpha(1 - \psi_I) / c_f^2} - 1\right]^2 . \tag{B.7}$$

The error introduced by approximations in Eq.(B.6-7) is small as long as Eq.(B.4) and $1 - \psi_I >> \Delta\psi_I$ are satisfied.